TDP-43 pathology links innate and adaptive immunity in amyotrophic lateral sclerosis

Baggio A. Evangelista[1,2]*, Joey V. Ragusa[2], Kyle Pellegrino[3], Yija Wu[4], Ivana Yoseli Quiroga-Barber[4], Shannon R. Cahalan[5], Omeed K. Arooji[1], Jillann A. Madren[6], Sally Schroeter[7], Joe Cozzarin[7], Ling Xie[8], Xian Chen[8], Kristen K. White[6], J. Ashley Ezzell[2], Marie A. Iannone[9], Sarah Cohen[2], Rebecca E. Traub[1], Xiaoyan Li[10], Richard Bedlack[10], Douglas H. Phanstiel[4], Rick Meeker[1], Natalie Stanley[11], Todd J. Cohen[1,2,8,12]*

[1]Department of Neurology, University of North Carolina, Chapel Hill, NC, USA
[2]Department of Cell Biology and Physiology, University of North Carolina, Chapel Hill, NC, USA
[3]Department of Pharmacology, University of North Carolina, Chapel Hill, NC, USA
[4]Department of Bioinformatics and Computational Biology, University of North Carolina, Chapel Hill, NC, USA
[5]Medical Student Training in Aging Research, Center for Aging and Health, University of North Carolina, Chapel Hill, NC, USA
[6]Microscopy Services Laboratory, Department of Pathology and Laboratory Medicine, University of North Carolina at Chapel Hill, Chapel Hill, NC, USA
[7]Standard BioTools Discovery Lab, Standard BioTools Inc., Markham, Ontario, CA
[8]Department of Biochemistry and Biophysics, University of North Carolina, Chapel Hill, NC, USA
[9]Lineberger Comprehensive Cancer Center, Department of Microbiology and Immunology, University of North Carolina, Chapel Hill, NC, USA
[10]Department of Neurology, Duke University Medical Center, Durham, NC, USA
[11]Department of Computational Medicine and Computer Science, University of North Carolina, Chapel Hill, NC, USA
[12]UNC Neuroscience Center, University of North Carolina, Chapel Hill, NC, USA

*Co-corresponding authors

Correspondence:

Todd J. Cohen, Ph.D. toddcohen@neurology.unc.edu

Baggio A. Evangelista, Ph.D. baevan@ad.unc.edu

Running Title: TDP-43 aggregates drive activation of innate and adaptive immune cells

Key Terms: ALS, TDP-43, neurodegeneration, neuroinflammation, innate immunity, adaptive immunity, microglia, T-cell, mass cytometry, imaging mass cytometry, RNA-sequencing, cytokine, immune synapse, antigen presentation

Abstract

Amyotrophic lateral sclerosis is the most common fatal motor neuron disease. Approximately 90% of ALS patients exhibit pathology of the master RNA regulator, Transactive Response DNA Binding protein (TDP-43). Despite the prevalence TDP-43 pathology in ALS motor neurons, recent findings suggest immune dysfunction is a determinant of disease progression in patients. Whether TDP-43 pathology elicits disease-modifying immune responses in ALS remains underexplored. In this study, we demonstrate that TDP-43 pathology is internalized by antigen presenting cells, causes vesicle rupture, and leads to innate and adaptive immune cell activation. Using a multiplex imaging platform, we observed interactions between innate and adaptive immune cells near TDP-43 pathological lesions in ALS brain. We used a mass cytometry-based whole-blood stimulation assay to provide evidence that ALS patient peripheral immune cells exhibit responses to TDP-43 aggregates. Taken together, this study provides a novel link between TDP-43 pathology and ALS immune dysfunction, and further highlights the translational and diagnostic implications of monitoring and manipulating the ALS immune response.

Introduction

ALS is the most common, fatal motor neuron disease worldwide. The disease is primarily characterized by the progressive degeneration of motor neurons in the motor cortex and spinal cord (1). The average post-diagnosis survival interval is approximately 2-5 years (2), however a subset of patients can survive >10 years post-diagnosis (3). Recent evidence suggests systemic immune perturbations modify ALS presentation and progression (4–6). Indeed, disparities in the levels of nearly every immune population including innate and adaptive immune cells have been documented in ALS (7–11). Additionally, loss-of-function mutations in several ALS-associated risk genes, such as C9ORF72 (chromosome 9 open reading frame 72) and TBK1 (TANK-binding kinase1) were shown to promote autoimmune-like inflammatory responses (12, 13). However, C9ORF72 and TBK1 mutations only constitute 5-7% and 1%, respectively, of all ALS cases (14, 15). In 2006, Neumann and colleagues identified pathological inclusions of TDP-43 as an underlying feature to motor neuron degeneration in the vast majority of nearly all ALS cases, including > 90% of those with sporadic ALS (16, 17).

TDP-43 regulates the expression or stability of approximately 6,000 transcripts across diverse biological processes in diverse cell types such as neuroglia and peripheral immune cells (18–22). In disease, TDP-43 mislocalizes to the cytoplasm and forms post-translationally modified aggregates (23–25). We recently

61 demonstrated that TDP-43 aggregates generated in human cells and then isolated by biochemical methods
62 contained nearly 2,000 sequestered proteins. These include classically defined damage associated molecular
63 patterns (DAMPs) such as heat shock proteins, heterogeneous nuclear ribonucleoproteins, and nuclear pore
64 proteins. We also demonstrated that monocyte-derived macrophages and microglia internalize TDP-43
65 aggregates (26). Other studies have shown that TDP-43 dysfunction leads to dysregulation of STING antiviral
66 immune responses in neurons (27). Here, we aimed to address the following question: do pathological TDP-43
67 species serve as antigens that stimulate disease-modifying immune cells that are relevant to ALS?

68 **Results**

69 **TDP-43 aggregates are phagocytosed, trafficked to autophagolysosomes, and promote acute activation**
70 **of primary monocyte-derived macrophages**

71 Our prior study showed that immunopurified, human TDP-43 aggregates (referred to as **TDP-43a**) are readily
72 internalized by both primary murine microglia and primary human monocyte-derived macrophages (hMDM)(26).
73 Additionally, we noted transcriptional similarity between human microglia and our hMDM cultures (28). For this
74 reason, we used hMDM for studying interactions with TDP-43a. We first assessed the dynamics of TDP-43a
75 internalization using biochemical methods. By immunoblot, we observed significant dose-dependent aggregate
76 internalization by hMDM following stimulation with TDP-43a at 0.025% (**$p = 0.0051$) and 0.1% (****$p < 0.0001$)
77 (Figure 1A). Laser-scanning confocal microscopy confirmed internalization via active, actin-dependent transport
78 (Figure 1B). These results suggest that actin-dependent phagocytosis is the dominant mode of TDP-43a
79 internalization. However, several internalization pathways could employ actin-polymerization. Thus, to
80 conclusively assess phagocytosis as the dominant route by which TDP-43a is internalized, we used a panel of
81 pharmacological inhibitors to target different internalization routes. These included Dynasore to inhibit dynamin-
82 mediated endocytosis and 5-(N-ethyl-N-isopropyl)-Amiloride (EIPA) to inhibit micropinocytosis. Following
83 inhibition and stimulation with TDP-43a, we counterstained the hMDM cell membrane with wheat-germ agglutinin
84 (WGA) and quantified complete internalization using laser-scanning confocal microscopy (Figure 1C-D). With
85 respect to vehicle control (27.13% ± 3.528%), a partial inhibitory effect was observed with Dynasore (15.75% ±
86 2.84%; *$p = 0.018$) and EIPA (15.13% ± 2.88%; *$p = 0.011$); however, cytochalasin D treatment consistently
87 inhibited internalization with 100% efficacy (****$p < 0.0001$). This led us to assess the functional response of
88 hMDM to TDP-43a internalization using a systems-based proteomics approach.

We performed combinatorial secretome and proteomics analysis on hMDM cultures stimulated with TDP-43a for 16 hours and identified several features of macrophage activation in the global intracellular proteome and secretome. These included increased secretion of macrophage migration inhibitory factor (MIF) (Log_2fold = 3.84; FDR < 0.05) and IL-1 converting enzyme or caspase 1 (Log_2fold = 3.67; FDR < 0.05), and reduced secretion of immunosuppressive immune checkpoint molecule CD276 (Log_2fold = -2.14; FDR < 0.05), among others (Supplementary Tables S1A-B). By merging these data into a network analysis, we identified upregulated signaling pathways including actin remodeling, phagocytosis, and autophagy (Figure 1E). These findings confirm that extracellular TDP-43a augments innate immune signaling and scavenging pathways, supporting the 'DAMP-like' properties of TDP-43a.

TDP-43a compromises autophagy and promotes vesicle rupture

Our proteomics analysis highlighted autophagy as a significant response following TDP-43a stimulation. Given the intimate link between TDP-43 dysfunction and autophagic dysregulation (29), and the fact that autophagic dysregulation can drive maladaptive immune responses (30), we next interrogated TDP-43a trafficking and autophagic integrity in hMDM. We first performed immunofluorescence and Airyscan confocal imaging where we observed co-localization between TDP-43a and markers of early endosomes (Rab5) (Figure 2A). We then validated lysosomal targeting by performing live-cell imaging using the vesicle acidification probe, LysoTracker-Red. Indeed, we observed co-localization between TDP-43a and LysoTracker-positive vesicles (Figure 2B). Furthermore, Airyscan confocal imaging of hMDM stimulated with TDP-43a for 16 hours revealed the presence of LC3-positive autophagosomes co-localizing with galectin-3 and TDP-43a, suggesting TDP-43a burden promotes vesicle rupture and downstream vesicle turnover (Figure 2C)(31, 32). We further characterized the ultrastructural integrity of vesicles by transmission electron microscopy (TEM) of hMDM stimulated with TDP-43a for 1 hour and 16 hours to simulate acute and chronic exposures, respectively (Figure 2D). By 16 hours we observed greater incidences of irregular, enlarged vesicles. We also identified features of vesicle degradation and turnover, indicated by increased presence of multivesicular bodies (MVBs). These ultrastructural features were not present in unstimulated or 1-hour stimulated hMDM. To validate whether autophagic processing is abnormal in the presence of pathological TDP-43a, hMDM were stimulated with TDP-43a and lysates were collected at 0, 0.5, 4, 8, 16, and 24 hours. Lysates were then probed for markers of autophagic flux, LC3-I and LC3-II, to assess autophagy induction (Figure 2E). We noted a distinctive loss of both LC3B-I and LC3B-II, rather

117 than ratiometric loss of LC3B-I and gain of LC3B-II, which is indicative of dysregulated autophagy (33). Additional
118 readouts of autophagic dysfunction include increased expression of the autophagy adaptor p62 (34). Indeed,
119 increased p62 levels correlated with LC3B-I and LC3B-II between 8 and 24 hours (Spearman's $r > 0.4$) (Figure
120 2E). Together, these results suggest that TDP-43 pathology induces autophagic dysfunction and vesicular
121 damage characterized by the mobilization of the inflammatory lectin galectin-3.

122 **TDP-43a drives a reactive transcriptome in primary monocyte-derived macrophages**

123 To determine if TDP-43a elicited an innate immune response at the transcriptional level, we conducted RNA-
124 sequencing on hMDM treated with either PBS or TDP-43a for 12 hours. We identified 262 differentially expressed
125 genes (Figure 3A; DESeq2, $p < 0.01$, absolute fold change > 1.15), including those with known roles in innate
126 immune response including galectin-3, TLR4, CCL22, SIGLEC1, and complement receptor 1 (CR1). Additional
127 differentially expressed genes included signaling regulators JAK1 and STAT5B, suggesting broad immune
128 modulation following TDP-43a stimulation. We note that these changes were more targeted and specific (both
129 in number and magnitude) compared to a 6-day, 'chronic' amyloid beta oligomer ($_{o}A\beta_{1-42}$) stimulation (712
130 differentially expressed genes) and a more potent 12-hour lipopolysaccharide (LPS) stimulation (5940
131 differentially expressed genes) (Figure 3B; Supplementary Table S3A-C). TDP-43a gene expression differences
132 were distinct compared to $_{o}A\beta_{1-42}$, as only 48 genes showed a common stimulation-dependent regulation, and
133 among these, the magnitude of differential expression was unique between TDP-43a and $_{o}A\beta_{1-42}$ (Figure 3C).
134 Gene ontology (GO) clustering indicated that TDP-43a preferentially regulated innate immune responses
135 (cytokine production involved in immune response), blood cell differentiation (myeloid cell differentiation and
136 regulation of hematopoiesis) and interleukin-2 signaling (Figure 3D). Importantly, interleukin-2 signaling is a
137 major orchestrator of innate-to-adaptive immune activation, predominantly through T-cell activation and
138 maintenance. These data suggest that internalized TDP-43a can activate innate immune responses and thereby
139 influence the crosstalk between innate and adaptive immune cells.

140 **TDP-43a promotes global immunophenotypic changes**

141 Given that there are numerous immune cell types with the potential to phagocytose and react to TDP-43a, we
142 asked how broadly TDP-43a impacts the human immune landscape using *ex vivo* human immune cell cultures.
143 Based on our mechanistic studies of TDP-43a internalization in hMDM, we reasoned that any professional

144 phagocyte may internalize TDP-43a. To address this question, we optimized a novel mass cytometry-based
145 aggregate internalization assay, that we termed *Aggre*-Gate, in bulk PBMCs that allowed for simultaneous global
146 immunophenotyping and cell population-wide localization of TDP-43a (Figure 4A schematic). To monitor
147 localization of TDP-43a, aggregates were first coupled to a Tellurium-Maleimide adduct (130Te) and used to
148 stimulate bulk primary human PBMC cultures. We confirmed that our assay follows linear kinetics of
149 internalization in phagocytes such as classical monocytes by traditional Boolean gating (Figure 4B-C and
150 Supplementary Figure S4A-B). We next used Spanning-Tree Progression Analysis of Density-Normalized
151 Events (SPADE) to stratify PBMCs and overlay relative 130Te intensity to identify TDP-43a internalization on a
152 cell cluster-specific basis. We observed TDP-43a internalization by all available phagocytic and antigen
153 presenting cells in PBMC preparations, including classical monocytes (77.13% ± 3.19%; ****$p < 0.0001$) and
154 dendritic cells (65.28% ± 8.91%; ****$p < 0.0001$) by SPADE and manual analyses. Strikingly, this analysis
155 platform identified TDP-43a internalization in B-cells, an unconventional phagocyte implicated in both antigen-
156 presentation and antibody production (8.683% ± 3.63%; *$p = 0.0263$). Finally, as expected, classically described
157 non-phagocytic cells such as CD8 T-cells ($^{ns}p > 0.999$) and natural killer (NK) cells ($^{ns}p = 0.9978$) did not
158 significantly internalize TDP-43a (Figure 4E-F).

159 In parallel, our TDP-43a mass cytometry assay also allowed us to profile adaptive immune cell activation
160 following acute, 24-hour stimulation with TDP-43a. Our phenotyping strategy included markers of proliferation,
161 early activation, tissue residency/homing, and immune checkpoints (Table 4). Unless otherwise specified, CD4
162 and CD8 T-cell subsets refer to the TCRαβ subtype, as this is the predominant TCR responsible for antigen
163 recognition. Both CD4 and CD8 T-cell subsets exhibited significant reduction in surface expression of CD127
164 levels following TDP-43a treatment, which is associated with immune activation, increased effector activity, and
165 senescence (35–37). CD127 downregulation was evident in CD4 effector T-cells (-0.232 ± 0.06 transformed
166 intensity units; *$p = 0.0186$) (Figure 4G), CD4 central memory T-cells (-0.276 ± 0.09 transformed intensity units;
167 *$p = 0.0332$) (Figure 4H), CD8 effector T-cells (-0.225 ± 0.04 transformed intensity units; **$p = 0.0082$) (Figure
168 4I), and CD8 central memory T-cells (-0.261 ± 0.08 transformed intensity units; *$p = 0.0393$) (Figure 4J).

169 **TDP-43a stimulation promotes antigen presentation and activation of naïve T-cells**

170 Classically, protein-driven T-cell immunity requires an essential intercellular signaling event between
171 antigen presenting cells and naïve CD4 and/or CD8 T-cells before memory responses are established. This

activation can be monitored via transient intracellular calcium release within T-cells, which is the downstream result of T-cell receptor-mediated PKCγ1 signal transduction (38). To address antigen presentation capabilities of TDP-43a-primed innate immune cells, we first adopted an established co-culture assay using Raji Burkitt lymphoma and Jurkat T-cell lines (39). This model was chosen as Raji and Jurkat cell lines have compatible MHC and TCRs, a necessity when assessing classical antigen presentation (40). Raji B-cells were labeled with CellTracker DeepRed and stimulated with immunopurified TDP-43a or isotype control product for 16-hours. Jurkat T-cells were labeled with CellTracker green and added to Raji cultures for 45 minutes and labeled with phalloidin to detect actin-dense immune synapses that form at junctions between APC and T-cells. The frequency of actin-dense intercellular contacts was quantified using laser-scanning confocal microscopy (Figure 5A-B). Phytohemagglutinin (PHA) was used as a positive control to non-specifically activate Raji cells and encourage immune synapse formation. TDP-43a (3.507% ± 0.17%; ****$p < 0.0001$) and PHA (2.533% ± 0.27%; ****$p < 0.0001$) stimulated Raji cells exhibited significantly higher frequencies of actin-polarized cell clusters with Jurkat T-cells relative to isotype control (0.513% ± 0.25%). We note that TDP-43a-stimulated Raji cells showed an even higher level of synapse formation compared to PHA (**$p = 0.0049$). However, since PHA is not a peptide antigen, we cannot directly compare the antigenic potency between TDP-43a and PHA.

To further validate this finding in a primary human system, we used syngeneic macrophage-mononuclear cell co-cultures to ensure HLA haplotype compatibility to appropriately assess TCR signaling. In this paradigm, hMDM were stimulated with TDP-43a or isotype control material for 16-hours. In parallel, frozen, syngeneic peripheral blood mononuclear cells (PBMCs) were thawed and allowed to recover overnight. At the time of assay, PBMCs were labeled with CellTracker Green (CTG), co-cultured with macrophages for 45 minutes, and subsequently fixed and labeled with phalloidin prior to analysis by Airyscan confocal microscopy. Strikingly, we noticed the presence of CTG-positive macrophage synapses with TDP-43a treatment (Figure 5C), but a complete absence of CTG labeled cells in the isotype control treatment. The lack of synapses in the isotype control condition is likely due to the inability to elicit hMDM activation leading to reduced chemotactic cues that recruit CTG-positive PBMCs. Supporting this possibility, our secretome analysis revealed significant increase in a notable T-cell chemotactic factor, CXCL16 (Log2fold change 2.836, FDR < 0.05, *$p = 0.034$) following TDP-43a stimulation. We then performed a separate live-cell imaging analysis where mixed hMDM-PBMC cultures were imaged immediately following the addition of TDP-43a or isotype control product. Compared to control,

200 TDP-43a stimulated cultures exhibited robust migration of PBMCS to hMDM that were actively interacting with
201 aggregates visible by phase-contrast microscopy (Supplementary Video SV1). Taken together, these data
202 suggest hMDM stimulated with TDP-43a exhibit heightened chemo-attractive properties that induce recruitment
203 and engagement of adaptive immune cells.

204 Our data so far suggests that TDP-43 aggregates can drive immune synapses between antigen
205 presenting cells and adaptive immune cells in several co-culture models of TDP-43a stimulation. However, it is
206 still unclear whether immune synapse formation in response to TDP-43a leads to cellular activation. Since
207 sustained memory T-cell responses indicate prior activation of naïve T-cells, we asked whether TDP-43a drives
208 antigen presentation and activation of naïve T-cell populations.

209 To address this question, we turned to a sensitive live-cell calcium imaging and co-culture assay (Figure
210 5D schematic). A functional readout of T-cell activation during antigen presentation is the immediate release of
211 intracellular calcium following TCR engagement (38). Thus, we stimulated hMDM for 16 hours with TDP-43a or
212 isotype control product. In parallel, syngeneic naïve CD4 and CD8 T-cells were enriched by negative magnetic
213 activated cell sorting (MACS). Here, naïve T-cells are defined as CD45RO-, CD45RA+, CCR7+, and CD27+
214 (Supplementary Figure S5A). As a positive control, we included co-cultures where hMDM were stimulated with
215 HIV virions, a previously established method to induce hMDM-T-cell antigen presentation and calcium signaling
216 (41). Next, hMDM and either naïve CD4 or CD8 T-cells were co-cultured and immediately imaged for 45 minutes
217 to monitor migration, cellular contact, and calcium activity. Strikingly, we observed recruitment of T-cells to the
218 hMDM plasma membrane (Figure 5E). Following recruitment, T-cells formed transient immune synapses, and
219 elicited rapid intracellular calcium responses. Quantification of calcium spiking events revealed significant
220 increases in both naïve CD4 (0.634 spikes/minute; **p = 0.0062) and CD8 T-cells (0.698 spikes/minute; ***p =
221 0.0002) following co-culture with TDP-43a-stimulated hMDM relative to isotype control stimulations (0.308
222 spikes/minute) (Figure 5F). These findings suggest TDP-43a can drive naïve T-cell activation via contact-
223 mediated antigen presentation, and thus satisfy early requirements for formation of conventional memory T-cell
224 responses.

225 **Imaging mass cytometry reveals antigen presenting microenvironments in ALS brain**

226 To support our *in vitro* and *ex vivo* assays, we determined whether the molecular and cellular features of innate-
227 to-adaptive immune activation are present in the ALS brain. Using formalin-fixed paraffin embedded ALS and

228 control brain sections, we performed a high parameter imaging mass cytometry assay to enable the
229 simultaneous labeling of TDP-43 pathology (Figure 6A) as well as a panel of heterogenous brain cell types
230 including brain-resident immune cells (Figure 6B) using a 17-plex antibody panel that included functional markers
231 of antigen presentation and memory T-cells (Table 5). We observed *in vivo* features of innate and adaptive
232 immune activation in ALS tissue that recapitulated features identified *in vitro*. These included microenvironments
233 containing activated microglia (CD68+) associated with pathological TDP-43 (phosphor-serine 409/410) (Figure
234 6B, arrowheads). Additionally, we identified a subset of myeloid cells that were positive for CD163, a marker
235 associated with infiltrating macrophages (42), galectin-3, and MHC-II (HLA-DR). We also observed intercellular
236 contacts between galectin-3+, HLA-DR+, CD163+ myeloid cells and CD8 T-cells (Figure 6B, white arrows).
237 Interestingly, these CD8 T-cells were also positive for the memory T-cell marker CD45RO but were granzyme
238 B-negative, although granzyme B-positive lymphocytes negative for T-cell markers were identified in the gray
239 matter (Supplementary Figure S6).

240 **CD8 T-cell subpopulations show divergent responses to TDP-43a in ALS patients**

241 Our data thus far suggest TDP-43 pathology alters immunophenotypes both *in vitro* and *ex vivo*. However, it
242 remains unknown whether immune responses to TDP-43 pathology are clinically relevant. Therefore, we
243 interrogated the relationship between immune populations, TDP-43a reactivity, and clinical progression of ALS.
244 First, we employed a whole-blood immune profiling assay (Figure 7A), which allows us to analyze the entirety of
245 a patient's immune profile without fractionation and cryopreservation, which minimizes frequency artifacts in
246 sensitive cell types such as monocytes and NK cells (43). Furthermore, we were able to characterize
247 granulocytes that are typically absent during PBMC profiling protocols (44).

248 ALS patients were categorized as fast-progressing (ΔALSFRS/t > 1.0; n=6), standard-progressing (0.5 <
249 ΔALSFRS/t $\leq$ 1.0; n=8), and-slow progressing (ΔALSFRS/t $\leq$ 0.5; n=9) based on the rate of change to their
250 revised ALS functional rating scale (ALSFRS-R) calculated between clinical visits (Table 6). Per-patient immune
251 profiles assayed through mass cytometry were then analyzed with VoPo, a machine learning pipeline for
252 identifying immunological correlates of particular clinical outcomes (Stanley et al., 2020). Briefly, Vopo first
253 integrates cells across all profiled samples to identify a common set of cell-populations in an agnostic manner.
254 Frequencies and functional marker readouts within each of these uncovered populations can then be
255 systematically compared to identify distinct cell subtypes that may be protective against fast progression (45).

256 Our analyses of the patient cohorts included several patient group comparisons to highlight the most relevant
257 immune populations in each of the fast, standard, or slow progression categories (Figure 7B and Supplementary
258 Figure S7).

259 Using VoPo, we first compared whole-blood profiles between fast- and standard-progressing ALS
260 patients. Candidates were validated by manual gating and statistical analysis. We identified a statistically
261 significant increased frequency of the mucosal associated invariant T-cell/natural killer T-cell (MAIT/NKT) niche
262 in fast-progressing patients compared to standard-progressing patients (0.10% vs. 0.23% of CD45+ leukocytes,
263 respectively; *p = 0.0221, Mann-Whitney U test). Additionally, we observed a significant reduction in senescent
264 NK cells in fast-progressing patients (3.48% vs 2.16% of CD45+ leukocytes, respectively; **p = 0.0027, Mann-
265 Whitney U test) (Figure 7C). We next compared whole-blood profiles between standard- and slow-progressing
266 patients. We identified a significant increase in plasmacytoid dendritic cells (0.13% vs 0.24% of CD45+
267 leukocytes, respectively; *p = 0.0115, Mann-Whitney U test) and terminally differentiated CD8 T-cells re-
268 expressing CD45RA (21.07% vs 47.21% of CD8+ T-cells, respectively; *p = 0.0418, Mann-Whitney U test) in
269 slow-progressing patients relative to standard-progressing (Figure 7D). We observed an increasing trend (though
270 not significant) in myeloid dendritic cells (^{ns}p = 0.0549) and eosinophils (^{ns}p = 0.175, Mann-Whitney U test) in
271 slow-progressing patients relative to standard-progressing patients.

272 We next wanted to assess whether immune population differences can be used to segregate slow-,
273 standard-, and fast-progressing patients as a proof-of-principle for predictive modeling of ALS progression. To
274 do so, we performed principal component analysis on whole blood profiles. At this sample size, we identified
275 relative segregation of standard-progressing patients, while slow- and fast-progressing patients appeared to
276 cluster together (Figure 7E). In further support of this, VoPo analysis revealed a lack of differentiating signal
277 when comparing slow- against fast-progressing patients in several clusters, including the CD8 TEMRA cluster
278 (CD8 T-cell 1). However, signal in this cluster returned when we compared standard to non-standard profiles
279 (aggregated slow- and fast-progressing profiles), with enrichment in the non-standard progressing group (Figure
280 7F). Although slow- and fast-progressing patients had similar CD8 TEMRA profiles based on VoPo, we
281 suspected that this particular sub-population may be functionally distinct and/or uniquely regulated in slow-
282 versus fast-progressing subtypes. Indeed, CD8 TEMRA have been characterized as functionally dichotomous,
283 with cytotoxic and regulatory roles governed by the IL-7/CD127 (IL-7R) axis (45). We reasoned that *bona fide*

284 functional readouts of CD8 TEMRA activity would provide additional information for distinguishing between fast-
285 and slow-progressing immune profiles.

286 To test this, we performed a proof-of-concept clinical case assessment. We implemented a blinded
287 whole-blood stimulation and mass cytometry assay with the goal of capturing functional differences, rather than
288 population differences, of ALS CD8 TEMRA following stimulation with TDP-43a. We performed the assay on 3
289 different ALS donors, one each of a fast-, standard-, and slow-progressing patient, and 3 same-visit control
290 samples taken from either a caretaker or cohabitating donor that is considered environmentally matched to the
291 respective patient. This design allowed us to reference ALS responses against natural immunological variability
292 that might arise from different genotypes and environments. Patient and control whole blood were stimulated for
293 16-hours with TDP-43a or dimethyl sulfoxide (DMSO) to establish baseline. We first opted to assess markers of
294 CD8 TEMRA senescence, an inherent property of cytotoxic T-cells with regulatory and pathological implications
295 (45). Specifically, we calculated the ratio of proliferative (CD127+CD57-) to senescent-like (CD127-CD57+) CD8
296 TEMRA. Each ratio was normalized to the respective DMSO control. Notably, the slow-progressing patient
297 TEMRA exhibited a 2.74-fold increase (non-inferential) in conversion of proliferative CD127+CD57- cells to
298 CD127-CD57+ senescent-like TEMRA following stimulation with TDP-43a. This conversion was absent in the
299 matched control, as well as fast- and standard-progressing patients and respective controls (Figure 8A). Next,
300 we assessed expression changes of CD103 as a readout of tissue-residency, a property that can minimize or
301 exacerbate chronic tissue damage (46). Remarkably, the slow-progressing patient TEMRA population exhibited
302 the largest loss of CD103+ TEMRA (-2.75%; non-inferential), compared to controls, standard-progressing (-
303 0.76%; non-inferential) and fast-progressing (+0.14%; non-inferential) patients (Figure 8B). While this data
304 indicates proof-of-concept functional differences across all three disease progression states, we emphasize that
305 larger sample sizes for whole-blood stimulation and profiling will be required for future quantitative ALS biomarker
306 studies. These data suggest that ALS patients exhibit dichotomous immune responses to human TDP-43
307 pathology that may delineate slow-, standard-, and fast-progressing ALS patients. We note that, since TDP-43a
308 contains numerous co-aggregating factors that are targets of innate and adaptive immunity, the identity of the
309 specific antigen(s) triggering this response is not yet known. Regardless of the exact self-antigens, these data
310 warrant further investigation into TDP-43a reactivity and the potential for immune monitoring as a readout for
311 ALS phenotypes.

312 **Discussion**

313 We discovered a novel link between innate and adaptive immune activation in response to pathological TDP-
314 43a. It was recently demonstrated that ALS adaptive immune responses are restricted to self-proteins (8) and
315 not pure TDP-43 protein (47). Using physiologically relevant TDP-43 aggregates containing accessory co-
316 aggregating DAMPs that we isolated from human cells, we provide evidence that this pathological TDP-43
317 species acts like a classically defined antigen with potential to induce innate and adaptive immune activation.
318 We assessed the ability of TDP-43 aggregates to 1) serve as a substrate for innate immune cell scavenging, 2)
319 drive innate immune cell activation, 3) augment antigen presentation to naïve CD4 and CD8 T-cells, and 4) elicit
320 memory T-cell responses in ALS immune cells.

321 When TDP-43a was used to stimulate hMDM, we observed phagocytosis-dependent internalization that
322 correlated with general immune reactivity (i.e., release of pro-inflammatory factors such as caspase 1, MIF, and
323 CXCL16), vesicle rupture, and autophagic dysfunction. It remains to be explored whether this autophagic
324 dysfunction is a key event in the activation of *both* CD4 and CD8 T-cells described herein. Classically, cargo
325 destined for degradation via autophagy is loaded onto MHC-II for antigen presentation to CD4 T-cells.
326 Conversely, intracellular antigenic cargo is degraded via proteasome and loaded onto MHC-I via TAP for antigen
327 presentation to CD8 T-cells. In certain host-defense states, non-conventional presentation routes of internalized
328 cargo can lead to both class I and class II presentation. Such events are termed *cross-antigen presentation* and
329 are characterized by downstream activation of both CD4 and CD8 T-cells (48). Our observations that TDP-43a
330 promotes autophagic dysfunction and vesicle rupture as evidenced by galectin-3 imaging, TEM, proteomics
331 analyses, and biochemical assays, leads us to speculate that a vesicle escape mechanism may drive cross-
332 presentation naïve CD4 and CD8 T-cell activation and T-cell memory responses. While it has been shown that
333 TDP-43 pathology can compromise both autophagy and proteasomal processing in ALS-affected neurons,
334 further experiments in immune cells are warranted to assess this hypothesis.

335 Our RNA-sequencing data further validated the galectin-3 feed-forward pathway of innate immune
336 activation following vesicle rupture, including increased expression of *LGALS3* and *TLR4* transcript in hMDM
337 following TDP-43a stimulation. We also gleaned information regarding ALS immunophenotypes including
338 reduced *TGFβ* and *STAT5* transcript levels, factors necessary for maintenance of regulatory T-cells (49) that are
339 reduced in ALS patients and inversely correlate with autoimmune-type Th17 T-cells (50–52). Moreover, we

340 observed increased expression of *CCL22*, a homing cytokine for CCR4-expressing NKT cells (53–55), which our
341 VoPo analysis highlighted in fast-progressing ALS patients. Finally, GO Term analysis highlighted the IL-2
342 signaling, a major T-cell regulatory pathway, following TDP-43a stimulation. These data further support
343 intercellular, innate-to-adaptive immune signaling as a link between early innate responses to TDP-43a and
344 clinically relevant adaptive immune signatures in ALS patients.

345 Using multiple primary and cell culture models of antigen presentation, we demonstrated that TDP-43a
346 stimulation of antigen presenting cells formed immune synapses with T-cells (Figure 5). With respect to naïve T-
347 cells, we observed intracellular activation via calcium signaling, a hallmark event for TCR-mediated T-cell
348 activation and adaptive immunity. Our high parameter neuroimmune imaging platform highlighted intercellular
349 contacts between innate and adaptive immune cells surrounding TDP-43 pathology *in the ALS brain*. We
350 emphasize that the exact peptide(s) presented on MHC in these experiments are unidentified. At the moment,
351 we cannot 1) conclude what protein within the TDP-43 aggregate is responsible for eliciting this reaction, nor 2)
352 assume it is necessarily the *same* peptide sequence or protein source across human donors. Additional variables
353 could include the highly polymorphic nature of MHC and its impact on peptide-selection and presentation, or
354 natural variation of thymic selection against anti-self T-cells that may exist on an individualistic, disease-specific,
355 or disease subtype-specific basis. Nevertheless, these are certainly topics for future global immunomic studies.

356 Finally, we implemented machine learning to identify peripheral immune signatures among ALS patients
357 that were associated with ALS progression rates. Surprisingly, ALS subtype-specific immune populations
358 exhibited functional responses when stimulated with TDP-43 pathology. We were surprised to observe that,
359 relative to standard-progressing patients, both slow and fast-progressors exhibited increased representation of
360 various innate and adaptive immune populations, one of these being CD8 TEMRA cells. We note an overall
361 higher representation of CD8 TEMRA cells in ALS, which is in line with previous reports (8). However, we found
362 that CD8 TEMRA cells—typically regarded as terminally differentiated with high cytolytic potential—were
363 overrepresented in non-standard-progressing ALS patients. One consideration is that TEMRA cells could have
364 dichotomous, regulatory properties in slow progressors but cytotoxic properties in fast-progressors. For example,
365 if CD8 TEMRA cells can adopt senescent phenotypes (CD127-CD57+) and regress from sites of tissue
366 inflammation (CD103-), a patient may be protected from advanced ALS phenotypes. However, if CD8 TEMRA
367 maintain proliferative capacity (CD127+CD57-) and reside in the CNS (CD103+), then off-target tissue damage

368 may expedite disease progression. We therefore suggest implementation of functional assays, rather than solely
369 population-based assays, that may provide greater clinical utility when combined with standard profiling
370 approaches. By analyzing whole-blood, but not PBMCs, within 4-hours of a patient visit, we were able to identify
371 changes to NKT cells in fast-progressing ALS. Though larger sample sizes in the future are necessary to extend
372 these findings, we suspect that critical cellular and functional information may be lacking in cryopreserved PBMC
373 preparations (8, 56, 57). Very few studies have been able to evaluate NKT cells, which are significantly impacted
374 by cryopreservation damage following PBMC isolation and storage (43) (58). In summary, this study sheds light
375 on how TDP-43 proteinopathy may be intimately linked to immune dysfunction in ALS and further highlights
376 whole-blood immune assays as a potential precision-medicine approach for diagnosing and predicting clinical
377 features of ALS progression.

378 **Materials and Methods**

379 Reagents, cell lines, and cell culture

380 Raji Burkitt lymphoma cell line (ATCC, CCL-86) and Jurkat T-cell clone E6-1 (ATCC, TIB-152) were procured
381 from UNC Tissue Culture Facility (UNC-TCF). Cells were cultured in vented T-75 flasks in Roswell Park Memorial
382 Institute (RPMI) 1640 media (Thermo Scientific, A1049101) supplemented with 10% fetal bovine serum, 2.0 mM
383 L-glutamine, and 1X penicillin/streptomycin. Cells were maintained between 1.0-2.0x^{6} cells/mL. To passage,
384 cells were collected by centrifugation at 300X RCF for 5 minutes. The cell pellet was resuspended in 1.0 mL of
385 calcium/magnesium-free PBS and incubated at 37°C for 5 minutes. Cell suspension was strained through a 40-
386 micron nylon strainer, counted as above, and re-seeded to a fresh T-75 flask. For a complete list of key
387 resources, see Table 1.

388 Peripheral Blood Mononuclear Cell (PBMC) Isolation

389 PBMCs were isolated from de-identified buffy-coated leukocytes obtained from New York Blood Center (Long
390 Island City, NY) following screening against bacteremia and viremia. Briefly, anticoagulated blood (heparin or
391 ACD citrate as indicated) was diluted 1:1 with 1X sterile phosphate-buffered saline (PBS). Diluted blood was
392 overlaid atop Ficoll-Hypaque density gradient (Sigma, GE17-1440-02) and centrifuged at 120X RCF for 20
393 minutes with zero brake. Buffy coat was isolated, washed in 1X PBS, centrifuged as above twice, and cleared
394 with 1X erythrocyte (RBC) lysis buffer for 10 minutes with gentle agitation. Cleaned PBMCs were then washed

395 with 1X PBS, counted using Trypan Blue exclusion hemocytometry, and plated according to assay or
396 differentiation protocol. For storage of PBMCs, cells were cryopreserved in 10% DMSO in antibiotic-free media
397 containing 10% FBS (Sigma, F2442), and 2 mM L-Glutamine (Gibco, 25030-081) in Dulbecco's Modified Eagle
398 Media (DMEM; Gibco, 31-053-028).

399 Primary human monocyte-derived macrophage (hMDM) culture

400 Freshly isolated PBMCs were plated at a density of $1.0x^6$ cells/mL into ultralow adhesion plastic tissue culture
401 dishes (Corning CLS3473), glass bottom slides (Cellvis, C8-1.5H-N), or glass-bottom culture dishes (Nunc,
402 150680) in complete DMEM consisting of 10% FBS, 2.0 mM L-glutamine, 1X Penicillin/Streptamycin (Gibco,
403 15140122). Monocytes were allowed to adhere to substrate for 5 days at 37°C, 5% CO_2. At day 5 in culture,
404 media was exchanged with complete media plus 15 ng/mL carrier-free recombinant human granulocyte-
405 macrophage colony stimulating factor (rhGM-CSF; R&D, 215-GM-010/CF). Thereafter, differentiated
406 macrophages were maintained with half-volume media exchanges performed every other day.

407 TDP-43 aggregate purification

408 The following is an abridged protocol based on Evangelista et al., 2023. All buffers and plastics were sterile and
409 procedures performed in a laminar flow hood. Briefly, HEK293A (ATCC, CRL1573) cells (ATCC, CRL1573) were
410 seeded to 15-cm tissue culture plates such that they reached 80% confluence at day of transfection. Cells were
411 transfected with 8 µg of pcDNA3.1-GFP-mNLS-K145Q using Fugene 6 Transfection reagent (Promega, E2692)
412 per manufacturer protocol. Cells were harvested 48-hours post-transfection in sterile 1X RIPA buffer
413 supplemented with protease, phosphatase, and RNAse inhibitors (Proega, PRN2111). Cells were passed
414 through 18-, 21-, and 25-gage syringes, vortexed at top speed for 30 seconds, and then treated with RQ1 RNAse-
415 free DNAse (Promega, M6101) for 30 minutes at 37°C. Sarkosyl was added to a final concentration of 0.5%.
416 Lysates were sheared as above, then centrifuged at 100,000X RCF for one hour at 4°C. The supernatants were
417 removed. Crude pellets were stored at -80 indefinitely until immunoprecipitation. To prepare immunoprecipitation
418 matrix, 30 µL of Protein A/G magnetic agarose (Thermo Scientific, 78609) was incubated with 15 µg of TDP-43
419 antibody (Proteintech, 10782-2-AP) for one hour at 4°C. Residual antibody was removed, beads were washed
420 twice with 1X RIPA, and twice with 1X PBS. BS3 cross-linker (Thermo Scientific, 21580) was diluted to 5 mM
421 with 1X sterile PBS. Antibody-bead complexes were crosslinked for 30 minutes at room temperature on an orbital

422 shaker. Crosslinking was quenched with a 1:10 ratio of 1.0 M Tris pH 7.5. Non-crosslinked antibody was removed
423 with 2 washes of Pierce Gentle Antibody elution buffer (Thermo Scientific, 21013), and the beads washed twice
424 more with 1X RIPA. Beads were then blocked overnight in non-protein block buffer (Licor Bioscience, 927-60001)
425 with 1mM DTT and 1.0% Tween-20 at 4°C with orbital rotation. For control samples, Rabbit isotype control
426 antibody was used in place of 10782-2-AP. To immunoprecipitated TDP-43 aggregates, pellets were retrieved
427 from -80°C. and sonicated in 500 µL of extraction buffer (1X RIPA supplemented with 0.5% Sarkosyl, 1.0%
428 Tween-20, 1.0 mM DTT, protease, phosphatase, and RNAse inhbitors). Bead slurry and lysate were combined
429 and allowed to bind overnight at 4°C with constant rotation. The next day, supernatants were removed, beads
430 were washed 3X in extraction buffer, and aggregates were eluted with a 3-series wash with 5.0 M NaCl warmed
431 to 55°C. Aggregates were pelleted at 100,000x RCF for 1 hour, and sonicated into a 1.0 mL solution (15 second
432 pulses, 30 second intermission on ice, for 4 cycles) using sterile 1X PBS unless otherwise specified.

433 Immunofluorescence analysis

434 Coverslips were gently rinsed in room temperature PBS and then immediately fixed in fresh, 4.0%
435 paraformaldehyde (PFA; Electron Microscopy Services, 15713S) for 10 minutes at room temperature. Cells were
436 rinsed 3X in PBS, then permeabilized using 0.2% Triton X-100 in PBS for 8 minutes at room temperature. Cells
437 were blocked in 2.0% normal goat serum (Sigma, NS02L-1ML) + 0.2% Triton X-100 (PBSTN) for one hour at
438 room temperature. Cells were incubated with primary antibodies in 2.0% PBSTN overnight at 4°C. Cells were
439 rinsed in PBST and subsequently stained with fluorophore conjugated secondary antibodies in PBSTN for one
440 hour at room temperature protected from light. Cells were preserved in ProLong Diamond anti-fade mounting
441 medium (Thermo Scientific, P36965).

442 hMDM aggregate uptake assay for confocal microscopy

443 hMDM were cultured in glass bottom dishes. Cells were pre-charged with 10 µM Cytochalasin D (Sigma, C8273),
444 80 µM Dynasore (Sigma, D7693), 10 µM EIPA (MedChem Express, HY-101840), or 0.05% DMSO control for 30
445 minutes at 37°C. Cells were then stimulated with 0.025% (v/v) TDP-43a and returned to incubator for 4 hours.
446 Cells were rinsed 1X in PBS, then immediately fixed for 10 minutes at room temperature with 4.0% PFA. Cells
447 were rinsed 2X in PBS and stained with 10 µg/mL Wheat-Germ Agglutinin (WGA) AlexaFluor 647 conjugate

448 (Invitrogen, W32466) for 10 minutes at room temperature. Cells were rinsed 2X in PBS and mounted with
449 ProLong Diamond antifade mounting media.

450 Confocal microscopy and live-cell imaging

451 Images were obtained on an inverted Zeiss 800/Airyscan laser-scanning confocal microscope fitted with 405,
452 488, 561, and 640 nm diode lasers and gallium arsenide phosphide (GaAsP) detectors. Live cells were incubated
453 in a 37°C heated stage in a humidified 5% CO_2 chamber. Image analyses were performed in FIJI (version 1.53t)
454 (59). Brightness and contrast were similarly adjusted between treatments.

455 Solubility fractionation and immunoblotting

456 6-well tissue culture plates were removed of media and rinsed 1X in 1.0 mL PBS. Cells were collected in 250 µL
457 of 1X radioimmunoprecipitation assay buffer (RIPA) by scraping over ice. In all cases, RIPA buffer was
458 supplemented with protease and phosphatase inhibitors. Lysates were sonicated 20-times at 25% amplitude
459 with a QSonica hand sonicator probe over ice. Samples were centrifuged at 21,000X RCF for 30 minutes at 4°C.
460 Supernatants were transferred to chilled microcentrifuge tubes and stored at -80°C as the soluble fraction. Pellets
461 containing insoluble fraction were resuspended in Urea plus protease and phosphatase inhibitors, and sonicated
462 for 10 pulses as above. Samples were centrifuged as above, and the supernatants stored as the insoluble
463 fraction. To prepare samples for sodium dodecyl sulfate polyacrylamide gel electrophoresis (SDS-PAGE)
464 analysis, protein lysate concentrations were normalized by bicinchoninic assay. 5.0-10.0 µg of protein lysate
465 were denatured in 1X reducing Laemmli buffer, boiled at 98°C for 5 minutes, and electrophoresed on 12% SDS-
466 PAGE gel. Proteins were transferred to nitrocellulose membrane at 4°C, 100V, for 75 minutes. Membranes were
467 blocked in Tris buffered saline-0.2% Tween (TBS-T) with 2.0% skim-milk for 30 minutes at room temperature
468 with rocking. Membranes were incubated with primary antibodies (Table 2) at 4°C overnight in 0.2% Milk-TBS.
469 Membranes were washed 3X in TBS-T, incubated with respective secondary antibodies (Table 3) for 60 minutes
470 at room temperature with rocking and washed as above. Membranes were imaged by enhanced
471 chemiluminescence and quantified using ImageStudo Lite.

472 Secretome and proteome analysis

473 Differentiated macrophages in 10-cm dishes underwent complete media change to serum-free DMEM. Cells
474 were then stimulated with 0.025% (v/v) aggregate-containing media or equal volume of isotype control material

475 and allowed to incubate for 16-hours. Cell culture media was removed and centrifuged at 300 RCF for 5 minutes
476 at 4°C to remove cell debris, followed by filtration through a 0.2 µm syringe filter. Cells were harvested by gently
477 scraping in ice-cold PBS, centrifuged as above and supernatant was removed. All components were then stored
478 at -80°C until a full set of replicates was obtained. For media analysis, proteins were precipitated with
479 deoxycholate and trichloroacetic acid. Next, protein precipitates and cell pellets were solubilized in 8M urea.
480 Proteins were then reduced, alkylated, and digested with Trypsin at room temperature overnight. Digested
481 peptides were then acidified with trifluoroacetic acid, desalted, and reconstituted in 0.1% formic acid. Samples
482 were analyzed by reverse phase liquid chromatography (LC)-MS/MS using Velos Orbitrap mass spectrometer
483 (Thermo). Experiments were calibrated to a mass accuracy of < 0.05.

484 Electron Microscopy

485 Adherent cells were fixed in 2% paraformaldehyde/2.5% glutaraldehyde in 0.15 M sodium phosphate buffer, pH
486 7.4 for 1 hour at room temperature, then stored in fixative at 4°C until processed for TEM. Fixative was aspirated
487 and cells were washed three times in 0.15 M sodium phosphate buffer. After washing, reduced osmium tetroxide
488 (1% osmium tetroxide with 1.25% potassium ferrocyanide in 0.15 M sodium phosphate buffer) was added to
489 cover the cellular monolayer and incubated at room temperature for 1 hour. Cells were washed three times with
490 deionized water and dehydrated through an ascending series of ethanol (30%, 50%, 75%, 90%, 100%, 100%
491 100%). They were then infiltrated with three exchanges of Polybed 812 epoxy resin (Polysciences, Inc.,
492 Warrington, PA) before being embedded in fresh 100% Polybed 812 epoxy resin and allowed to cure at 60°C
493 until hardened. Resin blocks were sectioned at 80 nm using a diamond ultra knife on a Leica UCT7
494 ultramicrotome and mounted on 200 mesh copper grids. Grids were stained with 4% aqueous uranyl acetate for
495 12 minutes followed by Reynold's lead citrate for 8 minutes, based on Reynolds et al., 1963 (60). Samples were
496 viewed using a JEOL JEM-1230 transmission electron microscope operating at 80 kV (JEOL USA, Inc.,
497 Peabody, MA) and images were obtained using a Gatan Orius SC1000 CCD Digital Camera and Gatan
498 Microscopy Suite 3.0 software (Gatan, Inc., Pleasanton, CA).

499 RNA Sequencing

500 *RNA-seq library preparation.* Total RNA was extracted using RNeasy Mini Kit (QIAGEN) guided by the
501 manufacturer's instructions. Each sample's RNA concentration and RNA integrity number (RIN) were measured

502 using Qubit and Agilent Tapestation 4150 system. The depletion of ribosomal RNAs (rRNAs) and the generation
503 of stranded RNA-seq libraries were performed using KAPA RNA HyperPrep with RiboErase kit with 500 ng of
504 isolated RNA as input and following the guidelines. Final libraries were quantified and normalized by Qubit and
505 DNA Tapestation and then combined to a total 4 nM library. The combined library was subsequently subjected
506 to paired-end 75bp read sequencing in the Illumina Nextseq550 platform.

507 *RNA-seq data analysis.* The quality of the reads was assessed by FastQC (version 0.11.9). Low-quality reads
508 and adapters were trimmed by using Trim Galore (version 0.6.7). The remaining reads were mapped to the hg19
509 transcriptome (GENCODE release19) and quantified by Salmon (v. 1.10.0). The estimated counts for each
510 sample were summarized by using tximport (v. 1.28.0). Differential gene analysis was applied to the counts
511 matrix with DESeq2 (v. 1.40.2) using a design adjusting for technical bias when calculating differences between
512 treatment groups (~Replicates+Condition). The method "apeglm" was used for effect size shrinkage (LFC
513 estimates). Genes with an FDR-adjusted p-value below 0.05 (Wald test) and an absolute fold change greater
514 than 1.15 were selected as the differential genes when comparing the treated samples to their corresponding
515 controls. The gene symbols and Entrez IDs were annotated to the data by using the package AnnotationHub (v.
516 3.8.0) and annotables (v. 0.2.0). The universal gene list and differential gene lists were then prepared for
517 generating functional enrichment results using over-representation analysis from the GO database by
518 clusterProfiler (v. 4.8.3), along with its complementary packages. The GO terms were identified with both FDR-
519 adjusted p-value and multiple testing corrected p-value lower than 0.05. The number of overlap genes between
520 different conditions was conducted by the package eulerr (v. 7.0.0) displaying the proportion of area related to
521 the numbers.

522 <u>Aggre-Gate: TDP-43a internalization assay by mass cytometry</u>

523 *^{130}Tellurium maleimide (130TeMal) coupling.* TDP-43a were purified as above. After the final spin, the
524 supernatant was removed and replaced with 500 µL of sterile Maxpar PBS, vortexed for 5 seconds, and collected
525 by centrifugation for 30 minutes at 100,000x RCF. The supernatant was removed and 100 mL of fresh sterile
526 Maxpar PBS was added. The pellet was sonicated for two cycles of 20, 1-second pulses at 25% amplitude with
527 a 30 second incubation on ice between cycles. Next, 1M DTT was added to a final concentration of 0.5 mM and
528 the sample partially reduced for 10 minutes at room temperature. The reaction was quenched with 900 µL of
529 sterile Maxpar Cell Staining Buffer (CSB), followed by centrifugation at 100,000 RCF for 30 minutes. The

530 supernatant was removed, replaced with 1.0 mL of sterile Maxpar PBS, vortexed, and centrifuged as above. The
531 partially reduced TDP-43a pellet was sonicated in 100 µL Maxpar PBS as above, and 1.1 µL of 10 mM 130TeMal
532 was added for a final concentration of 100 µM. Coupling occurred for 15 minutes at room temperature with
533 constant mixing by vortex at low speed. The reaction was quenched and centrifuged as above. 1.0 mL of sterile
534 PBS was added to the TDP-43a pellet and sonicated for two, 20-pulse cycles on ice as above. Aggregate
535 preparations were then tested for microbial and endotoxin contamination by culturing a sample in nutrient agar
536 followed by OD600 measurement (<0.001 arbitrary absorbance units) and LAL assay (<0.05 EU/mL),
537 respectively.

538 *Cell stimulations.* On Day 0, PBMCs were thawed in pre-warmed complete RPMI1640 supplemented with 50
539 units/mL of benzonase endonuclease. Cells were pelleted at 300x RCF for 3 minutes and the supernatant
540 discarded. Cells were resuspended in 5.0 mL of complete RPMI1640 plus benzonase and transferred to a vented
541 T-25 flask, allowed to recover overnight. The next morning, cells were collected by centrifugation. The cells were
542 resuspended in complete media to count viable cells by trypan blue exclusion. 2.0e6 cells were added to a 24-
543 well round-bottom tissue culture plate in complete RPMI. As indicated, TDP-43a was added to a final
544 concentration of 0.025% (v/v) and returned to 5% CO_2 incubation. Stimulations were performed in reverse
545 chronological order (i.e. starting with longest time-points) then collected at once for cytometry staining to
546 normalize phenotypic drift in bulk immune cultures along incubation.

547 *Mass cytometry staining and acquisition.* Following stimulation, cells were harvested in Maxpar PBS and
548 centrifuged at 300x RCF for 5 minutes. As needed, cells were barcoded using 1.0 µM TeMal and Selenium
549 maleimide (SeMal) barcodes in Maxpar PBS for 15 minutes at room temperature. TeMal isotopes were
550 synthesized by Dr.Youngran Seo at the University of North Carolina Department of Chemistry according to the
551 published protocol of *Willis et al* (61). Reactions were quenched with 3 volumes of CSB and centrifuged at 300x
552 RCF for 5 minutes. Cells were pooled in 100 µL volumes of CSB. Fc receptors were blocked with 10 µL TruStain
553 FCX receptor block (BioLegend, 422301) for 10 minutes at room temperature. Blocked cells were added to 110
554 µL of CSB and transferred to a Maxpar Direct Immunophenotyping Assay (MDIPA; Standard BioTools, 201334)
555 tube along with 50 µL of custom checkpoint antibody cocktail (For complete suspension mass cytometry antibody
556 panels see Table 4). Cells were stained for 30 minutes at room temperature. Cells were washed twice in 3.0 with
557 mL of CSB followed by centrifugation. Intracellular Ki67 staining was performed using the FoxP3 transcription

558 factor staining kit per manufacturer protocol (ThermoFisher, 00-5523-00). Cells were fixed in 2%
559 paraformaldehyde for 1 hour at 4°C, pelleted at 800X RCF for 7 minutes, and resuspended in 1.0 mL of Maxpar
560 Fix/Perm buffer containing 1:3000 Cell ID-Iridium DNA intercalator for overnight incubation at 4°C. The next day,
561 cells were pelleted at 800 RCF for 7 minutes, resuspended in 200 µL of Fix/Perm buffer, and stored at -80°C
562 until batch analysis. On day of analysis, cells were washed once with CSB, once with Cell Acquisition Solution
563 (CAS; Standard BioTools), then filtered through a 40-micron filter and diluted in CAS containing 10% EQ
564 Calibration Beads (Standard BioTools) at 0.5 million cells per mL and acquired on a mass cytometer (Helios).
565 Mass cytometry data were normalized using Fluigidm CyTOF software (v7.0). Sample files were pre-processed
566 to remove beads, debris, dead cells, and doublets for further downstream analysis. For SPADE analysis, down-
567 sampling was set to 10%, with a node setting of 75.

568 Raji-Jurkat immune synapse assay

569 Raji cells were stained with 1.0 µM Celltracker Deep Red (Invitrogen, C34565) for 30 minutes in supplement-
570 free RPMI1640 at 37°C. 2.0e6 cells were added to vented flow cytometry tubes in complete RPMI 1640. As
571 indicated 0.025% (v/v) TDP-43a, isovolumetric equivalent of isotype control material, or (0.5) µg/mL
572 phytohemagglutinin (PHA) were added to tubes for a 16-hour simulation period at 37°C. The next day, Jurkat T-
573 cells were incubated with 1.0 µM CellTracker Green (Invitrogen, C2925) for 30 minutes at 37°C. 2.0e6 Jurkat
574 cells were added to flow cytometry tubes containing Raji cells and incubated at 37°C for 45 minutes. Cells were
575 gently pipetted and strained through a 70 µm strainer directly into 1 volume equivalent of 8% PFA (for a final
576 concentration of 4%). Cells were fixed for 10 minutes at room temperature in the dark. Cells were pelleted at 800
577 RCF for 5 minutes, then resuspended in PHEM buffer (5 mM HEPES, 60 mM PIPES, 10 mM EGTA, 2 mM $MgCl_2$,
578 pH 7.0 with KOH) plus 0.1% (w/v) digitonin. To label immunological synapses, ActiStain-555 (phalloidin) was
579 added to a final concentration of 14 µM and incubated for 30 minutes at room temperature in the dark. Cells
580 were then rinsed in 1X PBS and incubated with 1ug/mL DAPI in PBS prior to mounting on microscope slides
581 with Prolong Diamond Antifade mounting media. Synapse frequencies were quantified as at least 1 Raji and 1
582 Jurkat T-cell containing a polarized actin contact site from randomized fields of view obtained on a 20X air
583 objective. Descriptively, synapses were then categorized as pair (one Raji per one Jurkat) or clusters.

584

585 Macrophage-PBMC co-culture assay

586 hMDM were sub-cultured to glass coverslips. hMDM were stimulated with 0.025% (v/v) immunopurified TDP-
587 43a and volumetric equivalent of isotype control product for 16 hours. In parallel, cryopreserved syngeneic
588 PBMCs were thawed and allowed to recover overnight in complete RPMI 1640 plus benzonase as above. The
589 next day, 2e6 PBMCs per condition were labeled with 1 μM CellTracker green for 30 minutes at 37°C in
590 supplement-free RPMI 1640. The reaction was quenched and washed with complete media. 1e6 labeled PBMCs
591 were added drop wise to stimulated hMDM and were returned to 37°C, 5% CO_2 for 45 minutes. Without disturbing
592 the cells, a 1-well volume equivalent of 8% PFA was added per well (final concentration 4%) and allowed to
593 incubate for 10 minutes at room temperature. Media was removed and fresh fixative was added for an additional
594 10 minutes. Coverslips were rinsed and permeabilized in PHEM buffer. Actin was stained using Acti-Stain 555
595 as above, nuclei were counter-labeled with DAPI, and immune synapses were imaged on an LSM 800 confocal
596 microscope at 20X and 63X magnification with Airyscan.

597 hMDM-T-cell calcium imaging assay

598 Macrophages were stimulated for 16-hours with 0.025% (v/v) TDiP aggregates or isovolumetric isotype control
599 material in complete media in Nunc glass-bottom microscope dishes. In parallel, naïve CD4 and CD8 T-cells
600 were isolated from syngeneic cryopreserved PBMC aliquots using the MojoSort magnetic negative selection kits
601 (BioLegend, 480041 and 480045). Naïve T-cells were incubated in complete medium supplemented with 10
602 IU/mL recombinant human IL-2 (R&D Systems, 202-IL-050/CF). As a positive control, macrophages were treated
603 with 10 pg/mL neutralized, CCR5 tropic, HIV virions. Following macrophage stimulations, macrophages and T-
604 cells were separately loaded with calcium indicator dye using a modified protocol. Here, cells were washed in
605 HEPES-buffered artificial cerebrospinal fluid (137 mM NaCl, 5 mM KCl, 2.3 mM $CaCl_2$, 1.3 mM $MgCl_2$, 20 mM
606 glucose, and 10 mM HEPES, pH 7.4) and pre-charged with 25% (v/v) Fluo-4 acetoxymethyl (Invitrogen, #
607 F14201) for 30 minutes. T-cells were added to macrophages at a ratio of 1 (macrophage) : 2 (T-cell) and imaged
608 on an Olympus IX71 inverted microscope. Time-lapsed images were measured every 6 seconds for 6 minutes
609 for 20 minutes using Metamorph (Molecular Devices). Change to fluorescence intensity was calculated using
610 baseline calcium levels per cell.

611

612 Qualitative Imaging Mass Cytometry

613 *Antibody Conjugation*. Antibody panel configuration was performed by Standard BioTools to ensure optimal
614 isotope assignment based on antigen abundance. Approximately 100 µg of each antibody (carrier- free) were
615 coupled to lanthanide metals using previously described protocols with the Maxpar X8 labeling kit (Standard
616 BioTools, 201169B). Briefly, antibodies were partially reduced with TCEP buffer (SBT, 77720) at 37°C. Following
617 112 reduction, antibodies were then incubated with an excess of metal-loaded MaxPar X8 polymer for 90 min at
618 37°C. Labeled antibodies were purified using a 50 kDa size exclusion centrifugal filter unit. Final antibody
619 concentration was determined by A_{280}. For complete list of IMC probes, refer to Table 5.

620 *Tissue staining*. 10 µM formalin-fixed paraffin embedded (FFPE) spinal cord sections from ALS and control spinal
621 patients were obtained from the Veterans Affairs ALS Brain Biorepository. FFPE sections were de-paraffinized
622 in xylene followed by progressive rehydration in a series of graded alcohols. Heat-induced epitope retrieval with
623 pH 9.0 buffer was performed prior to blocking in PBS + 3% BSA for 45 minutes. Tissues were then incubated
624 with antibodies overnight at 4°C in PBS + 0.5% BSA. Tissues were washed in PBS + 0.2% Triton X-100 prior to
625 nuclear staining with Iridium intercalator (1:800) for 30 minutes. Finally, tissues were washed with water and
626 dehydrated at room temperature. Regions of interest (ROI) were previously determined on an immediate serial
627 section using chromogenic immunohistochemistry, focusing on areas positive for pS409/410 (1D3). 1 mm x 1
628 mm ROIs were placed around 2 pS409/410-positive lesions. Synchronized laser ablation was performed at 200
629 Hz over a 2-hour period, generating regions with 1 μm^2 resolution. Data were exported to MCD Viewer (Standard
630 BioTools) where they were converted to 32-bit TIFF files. Each channel was despeckled and composite images
631 were created using FIJI (version 1.53t). Brightness and contrast for each marker was adjusted similarly across
632 each ROI.

633 Whole blood immune profiling and stimulation

634 *General immunophenotyping.* ALS patient blood was collected at Duke University and UNC Chapel Hill
635 Neurology clinics under approved Institutional Review. Blood was collected in 10 mL ACD citrate collection tubes
636 and processed within 4 hours of collection. 300 µL of anticoagulated blood were then added to one tube of the
637 Maxpar Direct Immunophenotyping Assay and incubated for 30 minutes at room temperature. Blood was briefly
638 agitated by tapping every 10 minutes to ensure even staining. Stained blood was then transferred to cryovials

639 containing 420 µL of SmartTube Proteomic Stabilizing agent (SmartTube Inc, 501351692), mixed, and allowed
640 to stabilize for 10 minutes at room temperature. Samples were then stored at -80°C until batch processing and
641 mass cytometry analysis. One day prior to analysis, stabilized blood was thawed at room temperature and
642 transferred to 10 mL of 1X Thaw/Lyse buffer (SmartTube Inc.) and allowed to incubate at room temperature for
643 10 minutes with orbital rotation. Lysed material was pelleted by centrifugation at 500 RCF for 5 minutes. Lysis
644 was repeated one time. Cells were then washed in 5 mL of CSB and resuspended in 1mL of 1X Maxpar PBS.
645 Cells were strained through 70 µM strainer caps into flow cytometry tubes containing 1 mL of 4% fresh PFA (final
646 concentration 2%). Cells were fixed for 1 hour at 4°C. Cells were pelleted at 800 RCF for 7 minutes, then
647 resuspended in 1 mL of Maxpar Fix/Perm buffer containing 1:3000 Cell-ID Iridium Intercalator. All samples
648 contained 500,000 universal donor PBMCs barcoded with 130TeMal to aid in normalization. A minimum of
649 300,000 events were collected in all conditions.

650 *Whole-blood TDP-43a stimulations.* For whole-blood stimulation assays, ALS and control patient blood was
651 collected in 5 mL Heparin tubes. We opted for heparin tubes as these appeared to be preferred for whole-blood
652 stimulation assays, although a comparative analysis suggests no significant difference in lymphocyte-antigen
653 response between ACD citrate and heparin (62). 300µL of blood was added to sterile vented flow cytometry
654 tubes and received either 3.0% (v/v) TDP-43a, 0.5 µg/mL PHA, or isovolumetric DMSO control that never
655 exceeded 0.05% in culture. Samples were incubated for 16-hours in 5% CO_2 at 37°C. Blood was transferred to
656 MDIPA reaction tubes with 50 µL of immune checkpoint antibody cocktail. A metal-minus-one control for CD103
657 gating was established by staining whole blood with MDIPA, excluding the CD103 probe. Following staining,
658 blood was stabilized, cleaned, and prepared for batch analysis as above.

659 Statistical analysis and data reporting

660 Where appropriate, data were assessed for normality by Kruskall-Wallis test. Non-parametric data were analyzed
661 by non-parametric two-tailed t-test, or multivariable Mann-Whitney U-test. Parametric data were analyzed by
662 two-tailed t-test, one-way ANOVA with Bonferroni correction or Tukey's multiple comparison test, or Two-way
663 ANOVA with Sidak's multiple comparison test. For correlation analysis, Spearman's *r* was used. For primary
664 PBMC stimulation data, paired t-tests were used to match genotypes. Arcsin(*h*) transformed data of surface
665 marker expression changes were analyzed via paired t-test. Statistical analysis was performed using GraphPad

Prism Version 9 for Windows (San Diego, CA). Cut-off for statistical significance were as follows: *p < 0.05, **p < 0.01, ***p < 0.001, ****p < 0.0001.

Contributions

B.A.E. conceptualized study, designed, and performed experimentation. J.V.R. and S.C. assisted in confocal microscopy experimentation and analysis. K.J.P and S.R.C. assisted in mass cytometry analysis and biochemical assays. O.K.A assisted in biochemical assays. J.M. and K.W. performed electron microscopy sample preparation and image acquisition. S.S., J.C., imaging mass cytometry panel design and image acquisition. L.X. and X.C. mass spectrometry analysis. J.A.E., histology. M.A.I, suspension mass cytometry panel design and sample acquisition. R.T., X.L., and R.B., patient care for study participants, managed clinical data, and sample acquisition. N.S., VoPo analysis of mass cytometry datasets. R.M. assisted with live-cell calcium imaging and analysis, and primary cell culture. T.J.C. supervised generation, acquisition, and analyses of all research data. B.A.E. wrote the manuscript, which was reviewed and edited by all co-authors.

Conflict of Interest

The authors declare no competing conflicts of interest.

Study Approval

The study was approved by the Institutional Review Pro00109640 of Duke University and 22-2638 of University of North Carolina at Chapel Hill. All participants were studied after providing written informed consent.

Acknowledgments

The Microscopy Services Laboratory, Department of Pathology and Laboratory Medicine, is supported in part by P30 CA016086 Cancer Center Core Support Grant to the UNC Lineberger Comprehensive Cancer Center. UNC Mass Cytometry Core University Cancer Research Fund (UCRF) UNC Cancer Center Core Support Grant P30CA016086. J.V.R. and S.C. were supported by the National Institute of General Medical Sciences of the National Institutes of Health under award number R35 GM133460. T.J.C. and was supported in part by National Institute of Neurological Disorders and Stroke R01 NS105981. D.H.P, I.Y.Q., Y.W., and T.J.C were supported in part by the National Institute of Aging R01 AG066871. Clinical work was supported in part by the North Carolina Translational and Clinical Sciences (TraCS) pilot award 550KR282107 awarded to R.T. and X.L. B.A.E was supported in part by the National Institute of Neurological Disorders and Stroke F31 NS122242. S.R.C was supported by National Institutes of Aging T35 AG038047. ALS tissue specimens were provided by the Department of Veterans Affairs Biorepository, VA Merit review BX002466. This work was supported by the Standard BioTools Discovery Lab at Standard BioTools Inc. Assay development such as staining, titrations, and data acquisition were performed as paid services. We'd like to thank N. Lane, K. Mottershead, R.J. Perna, A. Sidders, E. Swanson, for strategic discussion. We'd like to thank C. Simmons, M. Chopra, M. Ward, and H. Zampa for patient recruitment, enrollment, and sample acquisition. Finally, we sincerely thank the ALS patients and family members for their selfless contribution to this body of work.

Table 1. Key Resource Table

Reagent	Vendor	Catalogue
20% Paraformaldehyde	EMS	15713
ActiStain 555	Cytoskeleton Inc.	PHDH1
Bis-sulfosuccinimidyl suberate (BS3)	Thermo Scientific	21580
CellTracker Deep Red	Invitrogen	C34565

CellTracker Green CMFDA Dye	Invitrogen	C2925
Cytochalasin D	Sigma	C8273-1MG
DAPI	Invitrogen	D1306
Dimethyl Sulfoxide	Sigma	D2650
Dulbeccom's Modified Eagle Media	Gibco	31-053-028
Dynasore	Sigma	D7693-5MG
EIPA	MedChem Express	HY-101840
Fetal bovine serum	Sigma	F2442
Ficoll Paque Plus	Sigma	GE17-1440-02
Fluo-4-AM	Invitrogen	F14201
FoxP3 Fixation/Permeabilization kit	Thermofisher	Cat# 00-5523-00
Fugene 6 transfection reagent	Promega	E2692
HEK293A	ATCC	CRL1573
Human TruStain FcX	Biolegend	422301
Intercept (TBS) blocking buffer	Licor Bioscience	927-60001
Jurkat T-cell lymphoma clone E6-1	ATCC	TIB-152
L-glutamine	Gibco	25030-081
LysoTracker Deep Red	Invitrogen	L12492
Maxpar Direct Immunophenotyping Assay kit	Standard Biotools	201334
MojoSort Human CD4 Naïve T-Cell Isolation kit	BioLegend	480041
MojoSort Human CD8 Naïve T-Cell Isolation kit	BioLegend	480045
Phytohemagglutinin-L	Sigma	11249738001
Pierce Gentle Ag/Ab Elution buffer, pH6.6	Thermo Scientific	21013
Protein A/G magnetic Agarose	Thermo Scientific	78609
Raji B-cell lymphoma line	ATCC	CCL-86
rhGM-CSF	R&D Systems	215-GM-010/CF
rhIL-2	R&D Systems	202-IL-010
Roswell Park Memorial Institute 1640 media	Thermo Scientific	A1049101
RQ1 RNAse-Free DNAse I	Promega	M6101
Smart Tube Proteomic Stabilizer	SmartTube Inc.	501351692
SuperAsein RNAse inhibitor	Promega	PRN2111
Ultrafree cenrifugal filter, 0.1-micron	Sigma	UFC30VV25
Wheat Germ Agglutinin AlexaFluor 647 conjugate	Invitrogen	W32466

710

711 **Table 2. Primary antibodies**

Antibody	Vendor	Dilution	Catalogue	RRID
TDP-43 pS409/410	Proteintech	IB: 1:1000	80007-1-RR	AB_2882937

Total TDP-43	Proteintech	IB: 1:2000 TDiP: 40 µg	10782-2-AP	AB_615042
GFP	Aves	IB: 1:1000	GFP1202	AB_2734732
GAPDH	Millipore	IB: 1:1000	ABS16	AB_10806772
LC3B	CST	IB: 1:1000 IF: 1:100	2775S	AB_915950
p62	CST	IB: 1:1000	5114S	AB_10624872
Galectin-3	BioLegend	IF: 1:100	126701	AB_1134255
Rab5a	Santa Cruz	IF: 1:100	SC46692	AB_628191

712

713 **Table 3. Secondary antibodies**

Antibody	Vendor	Dilution	Catalogue
HRP Goat anti-Rabbit	Invitrogen	IB: 1: 3000	A31458
HRP Goat anti-Chicken	Invitrogen	IB:1: 3000	A16054
HRP Goat anti-Mouse	Invitrogen	IB:1:1000	A31430
AlexaFluor 594 conjugated goat anti-Rabbit	Invitrogen	IF: 1:500	A11012
AlexaFluor 594 conjugated goat anti-Mouse	Invitrogen	IF: 1:500	A32742
AlexaFluor 647 conjugated goat anti-Rabbit	Invitrogen	IF: 1:500	A32733

714

715 **Table 4. Suspension mass cytometry probes**

Assembly	Isotope	Antibody	Clone	Dilution
MDIPA Kit	89Y	CD45	HI30	
	141Pr	CD196/CCR6	G034E3	
	143Nd	CD123	6H6	
	144Nd	CD196/CCR6	HIB19	
	145Nd	CD4	RPA-T4	
	146Nd	CD8a	RPA-T8	
	147Sm	CD11c	Bu15	
	148Nd	CD16	3G8	
	149Sm	CD45RO	UCHL1	
	150Nd	CD45RA	HI100	
	151Eu	CD161	HP-3G10	
	152Sm	CD194/CCR4	L291H4	
	153Eu	CD25	BC96	
	154Sm	CD27	O323	
	155Gd	CD57	HNK-1	
	156Gd	CD183/CXCR3	G025H7	

	158Gd	CD185/CXCR5	J252D4	
	160Gd	CD28	CD28.2	
	161Dy	CD38	HB-7	
	163Dy	CD56/NCACM	NCAM16.2	
	164Dy	TCRgd	B1	
	166Er	CD294	BM16	
	167Er	CD197/CCR7	G043H7	
	168Er	CD14	63D3	
	170Er	CD3	UCHT1	
	171Yb	CD20	2H7	
	172Yb	CD66b	G10F5	
	173Yb	HLA-DR	LN3	
	174Yb	IgD	IA6-2	
	176Yb	CD127	A019D5	
	103Rh	Cell-ID Intercalator		
Expansion Panel	169Tm	CD69	FN50	0.125 µL/test
	165Ho	CD103	Ber-ACT8	0.125 µL/test
	159Tb	CD366	F38-2E2	2.0 µL/test
	162Dy	CD95	DX2	0.125 µL/test
	142Nd	CD134	ACT35	1.0 µL/test
	209Bi	CD137	4B4-1	1.0 µL/test
	175Lu	CD279	EH12.2H7	0.25 µL/test
	198Pt	Ki67	Ki-67	0.25 µL/test
	159Tb	HLA-ABC	W6/32	0.25 µL/test
Barcodes	76Se	76SeMal	In-house	Cell: 98 µM
	77Se	77SeMal	In-house	Cell: 98 µM
	78Se	78SeMal	In-house	Cell: 98 µM
	124Te	124TeMal	In-house	Cell: 2 µM
	126Te	126TeMal	In-house	Cell: 2 µM
	128Te	128TeMal	In-house	Cell: 2 µM
	130Te	130TeMal	In-house	Cell: 2 µM TDiP: 100 µM

716

717 **Table 5. Imaging mass cytometry probes**

Assembly	Isotope	Antibody	Clone	Dilution	Conjugation
Neural Landscape	150Nd	Total TDP-43	6H6E12	1:250	In-house
	159Tb	CD68	KP1	1:200	SBT
	161Dy	pS409/410 (pTDP-43)	1D3	1:100	In-house
	164Dy	GFAP	GA-5	1:700	In-house
	169Tm	Myelin Basic Protein	EPR21188	1:800	In-house
	194Pt	MAP2	MT-08	1:150	In-house
Immune Landscape	143Nd	CD45RA	HI100	1:200	In-house

	144Nd	CD31	EPR3094	1:50	In-house
	147Sm	CD163	EDHu-1	1:200	SBT
	153Eu	Mac2 (Galectin-3)	M3/38	1:50	SBT
	156Gd	CD4	EPR6855	1:200	SBT
	162Dy	CD8a	C8/144B	1:200	SBT
	167Er	Granzyme B	EPR20129-217	1:750	SBT
	170Er	CD3	Polyclonal	1:200	SBT
	173Yb	CD45RO	UCHL1	1:200	SBT
	174Yb	HLA-DR	LN3	1:50	SBT
	191/193Ir	DNA	N/A	1:800	SBT

Table 6. Patient demographics for whole-blood analysis

Identifier	Age of onset	Sex	ALSFRS-R/time*	Classifier	HIV	Riluzole*	Edaravone*	Sodium phenylbutyrate and taurursodiol*
Duke-812	78	F	0.60	Standard	no risks	no	no	no
Duke-813	78	F	0.15	Slow	no risks	yes	no	no
Duke-814	52	F	1.00	Standard	negative	no	no	no
Duke-815	61	F	0.70	Standard	no risks	yes	no	no
Duke-816	74	F	0.07	Slow	negative	no	no	no
Duke-817	60	M	0.42	Slow	no risks	no	no	no
Duke-818	79	M	0.37	Slow	no risks	yes	no	no
Duke-819	44	F	4.50	Fast	no risks	yes	no	no
Duke-824	65	M	0.38	Slow	negative	no	no	no
Duke-825	56	M	0.20	Slow	negative	no	no	no
Duke-826	73	M	1.40	Fast	negative	yes	no	no
Duke-827	61	M	1.40	Fast	no risks	yes	no	no
Duke-828	65	M	1.00	Standard	no risks	yes	no	no
Duke-829	55	F	0.40	Slow	no risks	no	no	no
Duke-830	68	M	0.74	Standard	negative	no	no	no
Duke-831	61	F	1.20	Fast	negative	no	no	no
Duke-832	59	F	2.20	Fast	negative	yes	no	no
Duke-835	75	M	0.50	Standard	negative	yes	no	no
Duke-836	67	M	0.60	Standard	negative	yes	yes	yes
Duke-838	74	F	0.35	Slow	no risks	no	no	no
UNC-003	72	M	0.00	Slow	no risks	yes	no	no
UNC-004	50	M	4.00	Fast	No risks	yes	yes	no

** At time of sample acquisition*

721 **Figure Legends**

722 **Figure 1. TDP-43 aggregates are phagocytosed, trafficked to autophagolysosomes, and promote acute**
723 **activation of primary human monocyte-derived macrophages. (A)** Immunoblot depicts the dose-dependent
724 uptake of insoluble, hyper-phosphorylated, GFP-tagged TDP-43a in primary hMDM**. (B)** Laser-scanning confocal
725 micrograph of early internalization of TDP-43a in primary hMDM counter-stained with phalloidin. Pseudo-colored
726 phalloidin stain depicts relative actin intensity. **(C)** Representative 3-dimensional renderings of complete and
727 incomplete TDP-43a internalization with respect to hMDM plasma membrane. Green denotes TDP-43a,
728 magenta denotes wheat-germ agglutinin. **(D)** Quantification of complete TDP-43a internalization in the presence
729 of phagocytosis inhibitor Cytochalasin D, endocytosis inhibitor Dynasore, and micropinocytosis inhibitor EIPA.
730 Data points depict the frequency of cells with at least one completely internalized TDP-43a particle relative to
731 the total number of cells in a randomized field of view. Color depicts data point with respect to donor genotype.
732 N = 3 independent experiments from 3 different genotypes. *P < 0.05, **P < 0.01, ***P < 0.001, ****P < 0.0001.
733 Ordinary one-Way ANOVA with Tukey's multiple comparison's test. Scale-bar 10-μm. **(E)** Volcano plots depict
734 differentially expressed intracellular (left) and secreted (middle) proteomes from primary hMDM cultures
735 stimulated with TDP-43a. Network analyses depict differentially expressed proteins related to phagocytosis
736 (upper right) and actin remodeling (lower right) pathways. Performed in triplicate (n = 3); FDR < 0.05; student's
737 *t*-test.

738 **Figure 2. TDP-43 aggregates compromise autophagy and promote vesicle rupture.** Airyscan and confocal
739 micrographs (630X) illustrate the extent of TDP-43a co-localization with early endosome marker Rab5a **(A)**,
740 acidified vesicle marker LysoTracker **(B)**, and ruptured autophagosome markers LC3B and Galectin-3 **(C)**. **(D)**
741 Transmission electron micrographs depict whole-cell hMDM (top left; scale-bar 10-μm, hMDM vesicles following
742 vehicle treatment (upper right; scale-bar 1-μm), and vesicles following TDP-43a treatment for 1-hour (lower left;
743 scale-bar 0.5-μm) and 16-hours (lower right; scale-bar 1-μm). Representative vesicles are shaded yellow. **(E)**
744 Representative immunoblots of LC3-I, LC3-II, and p62 kinetics in hMDM stimulated with TDP-43a. N = 2
745 independent experiments. Spearman's *r* correlation analysis of LC3B-I, LC3B-II, and p62 changes after
746 incubation with TDP-43a.

747 **Figure 3. Distinct and specific gene expression changes in primary human monocyte-derived**
748 **macrophages challenged with TDP43 aggregates. (A)** An MA plot depicts differential analysis of RNA-seq

749 data of cells treated with either TDP-43a or PBS for 12 hours. Differential genes are depicted in blue or red. **(B)**
750 A bar plot depicts the number of differential genes detected when comparing TDP-43a, AB, or LPS to cells
751 treated with PBS for the equivalent amount of time. Red represents upregulated genes and blue represents
752 down-regulated genes. **(C)** Gene Ontology enrichment analysis depicts functional gene clusters that were
753 enriched in those genes upregulated in response to 12 hours of TDP43a treatment. **(D)** Venn diagram depicting
754 unique and conserved genes that differentially expressed following TDP-43a or $_{o}A\beta_{1-42}$ treatment. Heat maps
755 depict the magnitude of expression change of each of the 48 conserved genes between TDP-43a and $_{o}A\beta_{1-42}$
756 treatments. Performed in duplicate, n = 2.

757 **Figure 4. Global immunophenotypic changes in response to TDP43 aggregates. (A)** Schematic of mass
758 cytometry-based TDP-43a internalization assay, *Aggre*-Gate. Purified TDP-43a is partially reduced with DTT
759 and coupled to Tellurium maleimide (^{130}TeMal) via thiol-reactive chemistry. Labeled TDP-43a are added to cell
760 cultures and internalization is determined by Boolean gating and/or Spanning-tree Progression of Density-
761 normalized Events (SPADE) following mass cytometry analysis. **(B)** Concatenated dot-plots depict kinetics of
762 TDP-43a internalization in classical monocytes from N = 3 independent cultures of a single genotype. **(C)** Linear
763 regression of the percent classical monocytes positive for TDP-43a with increasing incubation time with TDP-
764 43a**.** Gating scheme for identification of total monocytes is illustrated in Supplementary Figure 4B. **(E)**
765 Concatenated dot-plots of monocytes, dendritic cells, B-cells, natural killer (NK) cells, and CD8 T-cells positive
766 for TDP-43a. **(F)** Quantification of the percent of cells positive for TDP-43a following a 24-hour stimulation of
767 bulk PBMC from N = 3 genotypically unique donors (magenta, blue, and green datapoints). Analyzed by Two-
768 way ANOVA with Sidak's multiple comparison's test. Gating scheme for identification of immune cell subsets is
769 illustrated in Supplementary Figure 4B. **(G-J)** Quantification of relative CD127 expression levels as a readout of
770 T-cell effector activity following TDP-43a stimulation from N = 3 genetically unique donors. Arcsin(h) transformed
771 ratios of CD127 intensity across CD4 effector **(G)**, CD4 central **(H)**, CD8 effector **(I)**, and CD8 central **(J)** memory
772 T-cells. *P < 0.05, **P < 0.01, ***P < 0.001, ****P < 0.0001. Parametric, paired student's *t*-test.

773 **Figure 5. TDP-43 aggregates stimulate antigen presentation and activation of naïve T-cells. (A)**
774 Representative confocal micrographs (200X) of Raji-Jurkat synapses in the presence of isotype control (vehicle)
775 or TDP-43a purification products, or PHA. Pseudo-colored actin intensity images illustrate intercellular contacts
776 characterized by actin polarization. **(B)** Quantification of **A** by One-way ANOVA with Tukey's multiple

comparisons test. Graph depicts the frequency of cells forming contacts relative to the total number of cells in a randomized field of view. Data bars represent relative percentages of single and multiple cell contacts per condition, relative to the number of contacts in an image. Data points represent N = 3 independent passages. **(C)** Representative confocal micrographs (left; 200X) of primary hMDM immune synapses in the presence of isotype control (vehicle) or TDP-43a purification product. Arrowheads indicate hMDM (ActiStain-555; magenta) and arrows indicate regions of intercellular contact between hMDM and syngeneic PBMCs (CellTracker Green). High magnification Airyscan micrograph (right; 630X) illustrates actin-polarized contact between hMDM and PBMC (asterisk). **(D)** Schematic of live-cell calcium imaging co-culture assay to monitor naïve T-cell activation following TDP-43a stimulation of hMDM. **(E)** Time-series widefield fluorescence micrographs of intercellular contact between hMDM and naïve CD8 T-cell with intracellular calcium release. Dashed line denotes hMDM plasma membrane, and arrowheads denote site of intercellular contact. **(F)** Quantification of T-cell calcium signaling in both naïve CD4 and CD8 T-cell co-cultures with hMDM. Each data point represents single-cell calcium signaling events from a 40-minute imaging period within a single field of view. One field of view per coverslip. Inscribed values denote the total number of coverslips (n) analyzed across all genotypes (N). All data points originated from N = 3-5 unique genotypes. *P < 0.05, **P < 0.01, ***P < 0.001, ****P < 0.0001. Ordinary one-Way ANOVA with Dunnett's multiple comparisons test.

Figure 6. Imaging mass cytometry (IMC) profile of immune microenvironments near sites of TDP-43 pathology in ALS motor cortex. (A) Qualitative, representative overlays of the gray (left) and white (right) matter of motor cortex from a single control and ALS motor cortex tissue section. Insets represent magnified views of single feature markers for neurons (MAP2), TDP-43 pathology (pTDP-43), astrocytes (GFAP), and microglia (CD68). Nuclei counter-labeled blue. **(B)** Overlays and corresponding single-channel images of activated myeloid cells/microglia expressing antigen presentation machinery (Gal3, CD68, HLA-DR, CD163) and interacting with CD3+CD8+ T-cells in the parenchyma of ALS white matter. Nuclei counter-labeled blue. Vasculature marked with dashed line. Arrowheads denote pTDP-43 pathology, arrows denote interactions between antigen presenting cells, CD8 T-cells, and pTDP-43. Images were despeckled and adjusted similarly between control and ALS for brightness/contrast using FIJI.

Figure 7. Whole-blood immune profiling reveals niche immune populations that correlate with ALS progression-rate. (A) Schematic depicts whole-blood profiling strategy using computational and manual

805 analyses (top). Table summarizes sample sizes and progression rate classifiers determined using the rate of
806 change of the revised ALS functional rating scale (ALSFRS-R). **(B)** Annotated tSNE plot denotes immune sub-
807 populations and associated phenotyping markers of whole-blood leukocytes. **(C)** VoPo analyses and resulting
808 per-cluster enrichment scores between standard- and fast-progressing ALS patients. Quantification of manual
809 gating for NK cell 1 cluster and NKT cell cluster depicts reduced late natural killer cell frequencies (top) and
810 increased natural killer T-cells (bottom) in fast-progressing patients relative to standard-progressing patients.
811 Analyzed by Mann-Whitney U test. *P < 0.05, **P < 0.01, ***P < 0.001, ****P < 0.0001. **(D)** VoPo analysis and
812 cluster-specific enrichment scores between standard- and slow-progressing ALS patients. Quantification of
813 manual gating for dendritic cell cluster and CD8 T-cell cluster 1 depicts increased plasmacytoid dendritic cell
814 (top) and CD8 TEMRA cell (bottom) frequencies in slow-progressing patients relative to standard-progressing
815 patients. Analyzed by Mann-Whitney U test. *P < 0.05, **P < 0.01, ***P < 0.001, ****P < 0.0001. **(E)** Principal
816 component analysis of ALS whole-blood profiles depicts discrete clustering of standard- and non-standard (fast
817 + slow) patient whole-blood profiles. **(F)** VoPo analyses and resulting per-cluster enrichment scores between
818 slow- and fast-progressing patients (left) and standard- and non-standard-progressing patients (right). Circle
819 illustrates penetrance of CD8 TEMRA enrichment score in non-standard ALS patients.

820 **Figure 8. Clinical case assessment: TDP-43a whole-blood stimulation induces functional responses**
821 **that are dependent on disease progression rate. (A)** Normalized ratios of senescent (CD127-CD57+) to
822 proliferative (CD127+CD57-) CD8 TEMRA T-cells following TDP-43a stimulation of slow-, standard-, and fast-
823 progressing patient whole-blood cultures (top). Control samples are environmentally matched to each ALS
824 patient. Mass cytometry contour plots depict frequency changes of proliferative (magenta) and senescent
825 (green) CD8 TEMRA cells. Non-inferential, N = 1 patient and control pair, per progression-rate category. **(B)**
826 Percent difference of CD103+ CD8 TEMRA cells as a readout of tissue-homing potential following TDP-43a
827 stimulation of slow-, standard-, and fast-progressing patient whole-blood cultures (top). Control samples are
828 environmentally matched to each ALS patient. Mass cytometry contour plots depict CD103+ CD8 TEMRA cells
829 (cyan). Non-inferential, N = 1 patient and control pair, per progression-rate category.

830 **References**

831 1. Brown RH, Al-Chalabi A. Amyotrophic Lateral Sclerosis. *N Engl J Med*. 2017;377(2):162–172.

832 2. Huisman MHB, et al. Population based epidemiology of amyotrophic lateral sclerosis using capture-
833 recapture methodology. *J Neurol Neurosurg Psychiatry*. 2011;82(10):1165–1170.

834 3. Wijesekera LC, et al. Natural history and clinical features of the flail arm and flail leg ALS variants.
835 *Neurology*. 2009;72(12):1087.

836 4. Abu-Rumeileh S, et al. Diagnostic-prognostic value and electrophysiological correlates of CSF biomarkers of
837 neurodegeneration and neuroinflammation in amyotrophic lateral sclerosis. *J Neurol*. 2020;267(6):1699–1708.

838 5. Thonhoff JR, Simpson EP, Appel SH. Neuroinflammatory mechanisms in amyotrophic lateral sclerosis
839 pathogenesis. *Curr Opin Neurol*. 2018;31(5):635–639.

840 6. Masrori P, et al. The role of inflammation in neurodegeneration: novel insights into the role of the immune
841 system in C9orf72 HRE-mediated ALS/FTD. *Mol Neurodegener 2022 171*. 2022;17(1):1–23.

842 7. Murdock BJ, et al. NK cells associate with ALS in a sex- and age-dependent manner. *JCI Insight*.
843 2021;6(11). https://doi.org/10.1172/JCI.INSIGHT.147129.

844 8. Campisi L, et al. Clonally expanded CD8 T cells characterize amyotrophic lateral sclerosis-4. *Nature*.
845 2022;606(7916):945–952.

846 9. Choi SJ, et al. High neutrophil-to-lymphocyte ratio predicts short survival duration in amyotrophic lateral
847 sclerosis. *Sci Reports 2020 101*. 2020;10(1):1–6.

848 10. Rolfes L, et al. Amyotrophic lateral sclerosis patients show increased peripheral and intrathecal T-cell
849 activation. *Brain Commun*. 2021;3(3). https://doi.org/10.1093/BRAINCOMMS/FCAB157.

850 11. Cui C, et al. Correlation between leukocyte phenotypes and prognosis of amyotrophic lateral sclerosis.
851 *Elife*. 2022;11. https://doi.org/10.7554/ELIFE.74065.

852 12. McCauley ME, et al. C9orf72 in myeloid cells suppresses STING-induced inflammation. *Nature*.
853 2020;585(7823):96–101.

854 13. Oakes JA, Davies MC, Collins MO. TBK1: a new player in ALS linking autophagy and neuroinflammation.
855 *Mol Brain*. 2017;10(1):1–10.

856 14. DeJesus-Hernandez M, et al. Expanded GGGGCC hexanucleotide repeat in noncoding region of
857 C9ORF72 causes chromosome 9p-linked FTD and ALS. *Neuron*. 2011;72:245–256.

858 15. Renton AE, et al. A hexanucleotide repeat expansion in C9ORF72 is the cause of chromosome 9p21-
859 linked ALS-FTD. *Neuron*. 2011;72:257–268.

860 16. Deerlin VM Van, et al. TARDBP mutations in amyotrophic lateral sclerosis with TDP-43 neuropathology: a
861 genetic and histopathological analysis. *Lancet Neurol*. 2008;7:409–416.

862 17. Neumann M, et al. Ubiquitinated TDP-43 in fronto-temporal lobar degeneration and amyotrophic lateral
863 sclerosis. *Science (80-)*. 2006;314:130–133.

864 18. Buratti E, Baralle FE. Characterization and Functional Implications of the RNA Binding Properties of
865 Nuclear Factor TDP-43, a Novel Splicing Regulator of CFTR Exon 9. *J Biol Chem*. 2001;276(39):36337–
866 36343.

867 19. Buratti E, et al. TDP-43 binds heterogeneous nuclear ribonucleoprotein A/B through its C-terminal tail: An
868 important region for the inhibition of cystic fibrosis transmembrane conductance regulator exon 9 splicing. *J*
869 *Biol Chem*. 2005;280(45):37572–37584.

870 20. Buratti E, et al. Nuclear factor TDP-43 can affect selected microRNA levels. *FEBS J*. 2010;277(10):2268–
871 2281.

872 21. Colombrita C, et al. TDP-43 and FUS RNA-binding proteins bind distinct sets of cytoplasmic messenger
873 RNAs and differently regulate their post-transcriptional fate in motoneuron-like cells. *J Biol Chem*.
874 2012;287(19):15635–15647.

875 22. Polymenidou M, et al. Long pre-mRNA depletion and RNA missplicing contribute to neuronal vulnerability
876 from loss of TDP-43. *Nat Neurosci*. 2011;14(4):459–468.

877 23. Neumann M, et al. Ubiquitinated TDP-43 in frontotemporal lobar degeneration and amyotrophic lateral
878 sclerosis. *Science (80-)*. 2006;314(5796):130–133.

879 24. Arai T, et al. TDP-43 is a component of ubiquitin-positive tau-negative inclusions in frontotemporal lobar
880 degeneration and amyotrophic lateral sclerosis. *Biochem Biophys Res Commun*. 2006;351(3):602–611.

881 25. Baloh RH. TDP-43: The relationship between protein aggregation and neurodegeneration in amyotrophic
882 lateral sclerosis and frontotemporal lobar degeneration. *FEBS J*. 2011;278(19):3539–3549.

883 26. Evangelista BA, et al. Tandem detergent-extraction and immunoprecipitation of proteinopathy: Scalable
884 enrichment of ALS-associated TDP-43 aggregates. *iScience*. 2023;26(5):106645.

885 27. Yu CH, et al. TDP-43 Triggers Mitochondrial DNA Release via mPTP to Activate cGAS/STING in ALS.
886 *Cell*. 2020;183(3):636.

887 28. Quiroga IY, et al. Synthetic amyloid beta does not induce a robust transcriptional response in innate
888 immune cell culture systems. *J Neuroinflammation*. 2022;19(1). https://doi.org/10.1186/S12974-022-02459-1.

889 29. Budini M, et al. Autophagy and Its Impact on Neurodegenerative Diseases: New Roles for TDP-43 and
890 C9orf72. *Front Mol Neurosci*. 2017;10:170.

891 30. Qian M, Fang X, Wang X. Autophagy and inflammation. *Clin Transl Med*. 2017;6(1):24.

892 31. Jiang P, et al. Impaired endo-lysosomal membrane integrity accelerates the seeding progression of α-
893 synuclein aggregates. *Sci Rep*. 2017;7(1):7690.

894 32. Paz I, et al. Galectin-3, a marker for vacuole lysis by invasive pathogens. *Cell Microbiol*. 2010;12(4):530–
895 544.

896 33. Mizushima N, Yoshimori T. How to interpret LC3 immunoblotting. *Autophagy*. 2007;3(6):542–545.

897 34. Wu Y, et al. P62/SQSTM1 accumulation due to degradation inhibition and transcriptional activation plays a
898 critical role in silica nanoparticle-induced airway inflammation via NF-κB activation. *J Nanobiotechnology*.
899 2020;18(1):1–15.

900 35. Wu H, et al. Expression of KLRG1 and CD127 defines distinct CD8+ subsets that differentially impact
901 patient outcome in follicular lymphoma. *J Immunother cancer*. 2021;9(7). https://doi.org/10.1136/JITC-2021-
902 002662.

903 36. Lim HW, Kim CH. Loss of IL-7 receptor alpha on CD4+ T cells defines terminally differentiated B cell-

904 helping effector T cells in a B cell-rich lymphoid tissue. *J Immunol*. 2007;179(11):7448–7456.

905 37. Benito JM, et al. Down-regulation of interleukin-7 receptor (CD127) in HIV infection is associated with T cell
906 activation and is a main factor influencing restoration of CD4(+) cells after antiretroviral therapy. *J Infect Dis*.
907 2008;198(10):1466–1473.

908 38. Trebak M, Kinet JP. Calcium signalling in T cells. *Nat Rev Immunol 2018 193*. 2019;19(3):154–169.

909 39. Bello-Gamboa A, et al. Imaging the Human Immunological Synapse. *J Vis Exp*. 2019;2019(154).
910 https://doi.org/10.3791/60312.

911 40. Fukumoto R, et al. Inhibition of T-cell receptor signal transduction and viral expression by the linker for
912 activation of T cells-interacting p12(I) protein of human T-cell leukemia/lymphoma virus type 1. *J Virol*.
913 2007;81(17):9088–9099.

914 41. Killebrew DA, et al. Suppression of HIV-associated Macrophage Activation by a p75 Neurotrophin Receptor
915 Ligand. *J Neuroimmune Pharmacol*. 2022;17(1–2):242–260.

916 42. Fabriek BO, Dijkstra CD, van den Berg TK. The macrophage scavenger receptor CD163. *Immunobiology*.
917 2005;210(2–4):153–160.

918 43. Li B, et al. Comprehensive evaluation of the effects of long-term cryopreservation on peripheral blood
919 mononuclear cells using flow cytometry. *BMC Immunol*. 2022;23(1). https://doi.org/10.1186/S12865-022-
920 00505-4.

921 44. Jaatinen T, Laine J. Isolation of mononuclear cells from human cord blood by Ficoll-Paque density
922 gradient. *Curr Protoc Stem Cell Biol*. 2007;Chapter 2. https://doi.org/10.1002/9780470151808.SC02A01S1.

923 45. Stanley N, et al. VoPo leverages cellular heterogeneity for predictive modeling of single-cell data. *Nat*
924 *Commun 2020 111*. 2020;11(1):1–9.

925 46. Smolders J, et al. Tissue-resident memory T cells populate the human brain. *Nat Commun 2018 91*.
926 2018;9(1):1–14.

927 47. Ramachandran S, et al. Low T-cell reactivity to TDP-43 peptides in ALS. *Front Immunol*. 2023;14.
928 https://doi.org/10.3389/FIMMU.2023.1193507/FULL.

929 48. Pishesha N, Harmand TJ, Ploegh HL. A guide to antigen processing and presentation. *Nat Rev Immunol*.
930 2022;22(12):751–764.

931 49. Passerini L, et al. STAT5-signaling cytokines regulate the expression of FOXP3 in CD4+CD25+ regulatory
932 T cells and CD4+CD25- effector T cells. *Int Immunol*. 2008;20(3):421–431.

933 50. Beers DR, et al. ALS patients' regulatory T lymphocytes are dysfunctional, and correlate with disease
934 progression rate and severity. *JCI Insight*. 2017;2(5). https://doi.org/10.1172/JCI.INSIGHT.89530.

935 51. Rentzos M, et al. Interleukin-17 and interleukin-23 are elevated in serum and cerebrospinal fluid of patients
936 with ALS: a reflection of Th17 cells activation? *Acta Neurol Scand*. 2010;122(6):425–429.

937 52. Saresella M, et al. T helper-17 activation dominates the immunologic milieu of both amyotrophic lateral
938 sclerosis and progressive multiple sclerosis. *Clin Immunol*. 2013;148(1):79–88.

939 53. Kim CH, Johnston B, Butcher EC. Trafficking machinery of NKT cells: shared and differential chemokine
940 receptor expression among Vα24+Vβ11+ NKT cell subsets with distinct cytokine-producing capacity. *Blood*.
941 2002;100(1):11–16.

942 54. Semmling V, et al. Alternative cross-priming through CCL17-CCR4-mediated attraction of CTLs toward
943 NKT cell-licensed DCs. *Nat Immunol*. 2010;11(4):313–320.

944 55. Yoshie O, Matsushima K. CCR4 and its ligands: from bench to bedside. *Int Immunol*. 2015;27(1):11–20.

945 56. Yazdani S, et al. T cell responses at diagnosis of amyotrophic lateral sclerosis predict disease progression.
946 *Nat Commun*. 2022;13(1). https://doi.org/10.1038/S41467-022-34526-9.

947 57. Yildiz O, et al. Senescent-like Blood Lymphocytes and Disease Progression in Amyotrophic Lateral
948 Sclerosis. *Neurol Neuroimmunol neuroinflammation*. 2022;10(1).
949 https://doi.org/10.1212/NXI.0000000000200042.

950 58. Rentzos M, et al. Alterations of T cell subsets in ALS: a systemic immune activation? *Acta Neurol Scand*.
951 2012;125(4):260–264.

952 59. Schindelin J, et al. Fiji: an open-source platform for biological-image analysis. *Nat Methods 2012 97*.
953 2012;9(7):676–682.

954 60. REYNOLDS ES. The use of lead citrate at high pH as an electron-opaque stain in electron microscopy. *J*
955 *Cell Biol*. 1963;17(1):208–212.

956 61. Willis LM, et al. Tellurium-based mass cytometry barcode for live and fixed cells. *Cytom Part A*.
957 2018;93(7):685–694.

958 62. Chuenchitra T, et al. A whole blood lymphocyte proliferation assay in healthy Thais: comparison of
959 heparinized blood and acid citrate dextrose blood. *J Med Assoc Thai*. 2010;93 Suppl 2:S21-6.

960

Figure 1

Evangelista et al., 2024

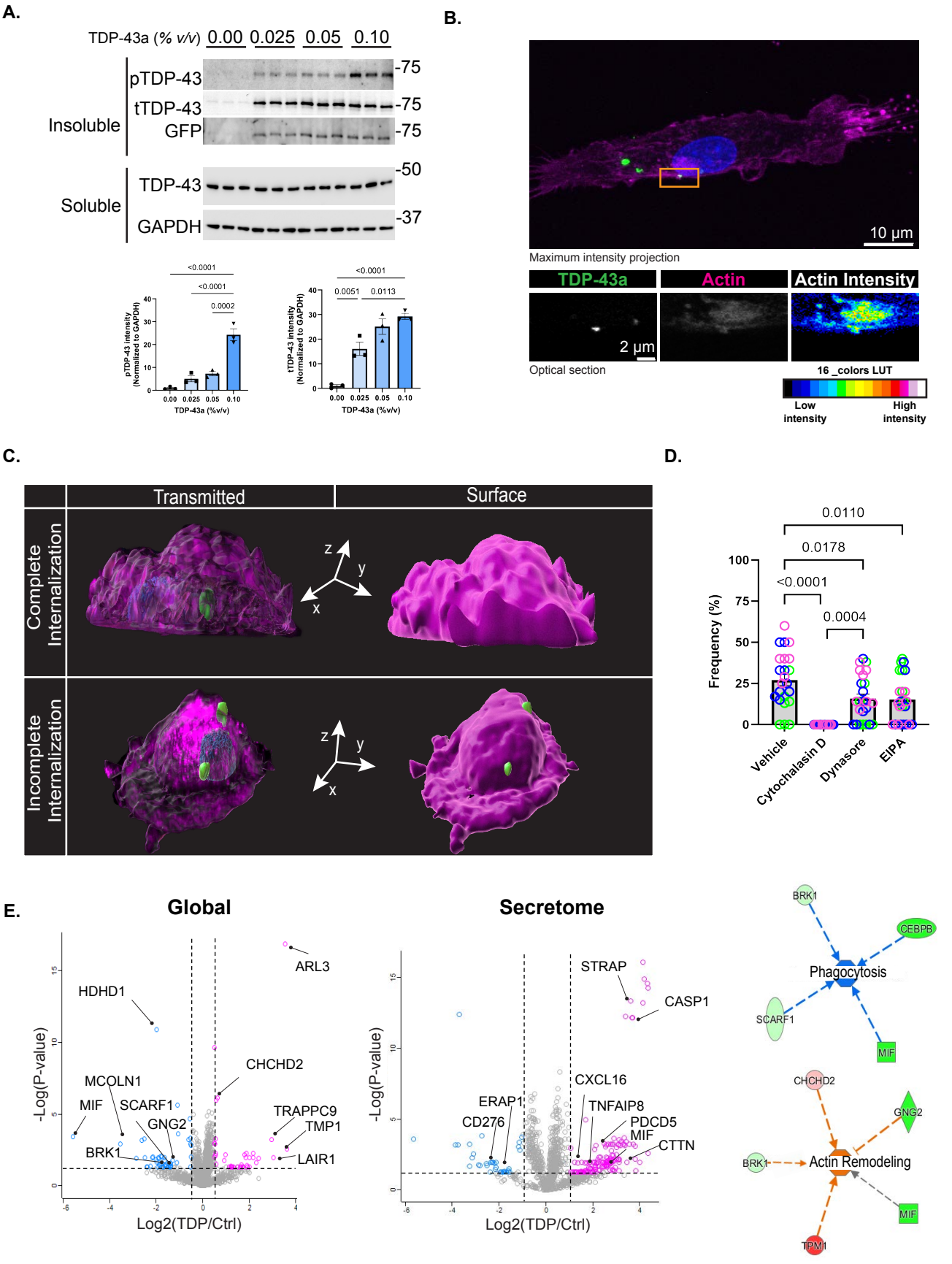

Figure 2

Evangelista et al., 2024

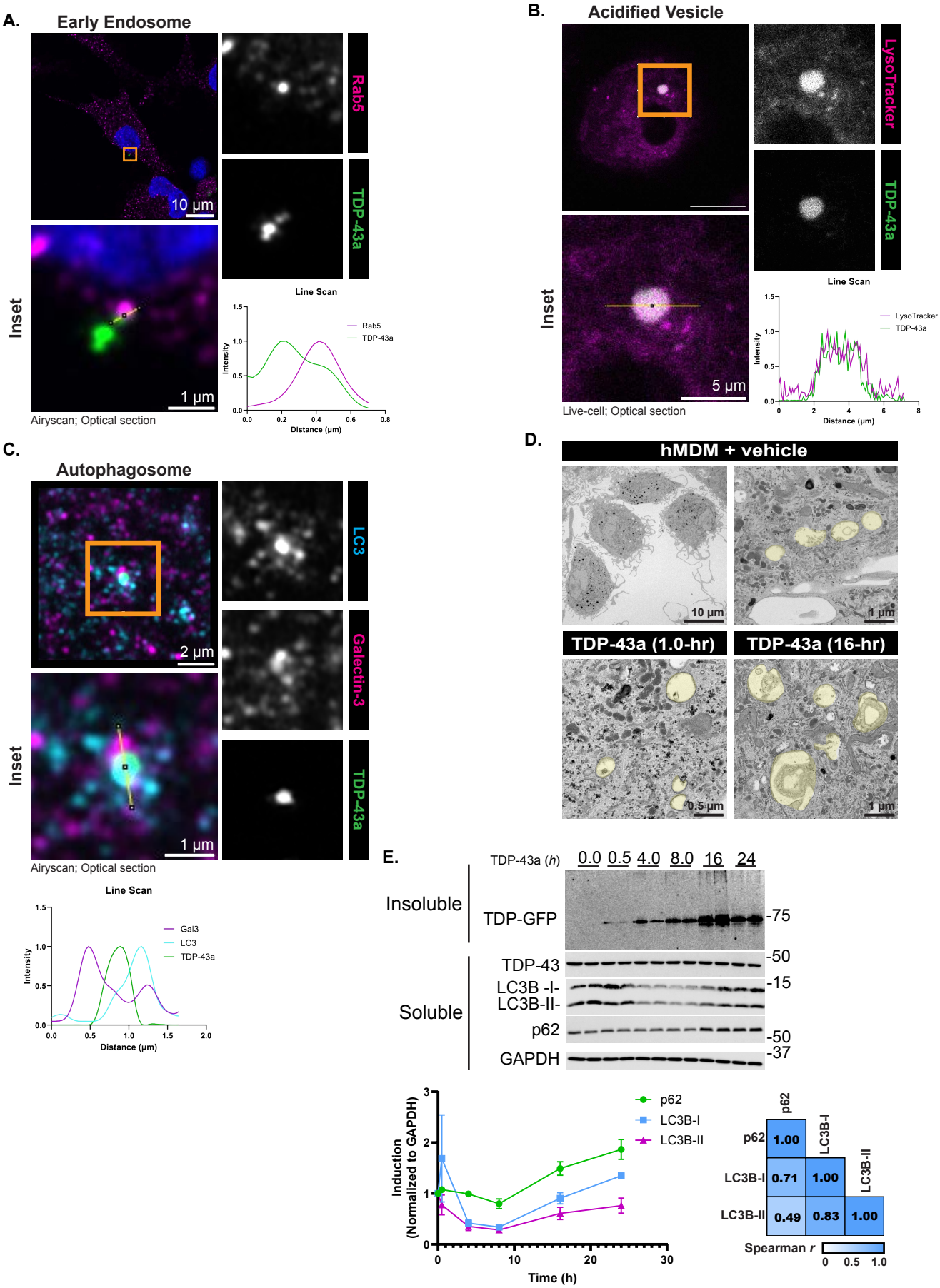

Figure 3

Evangelista et al., 2024

A.

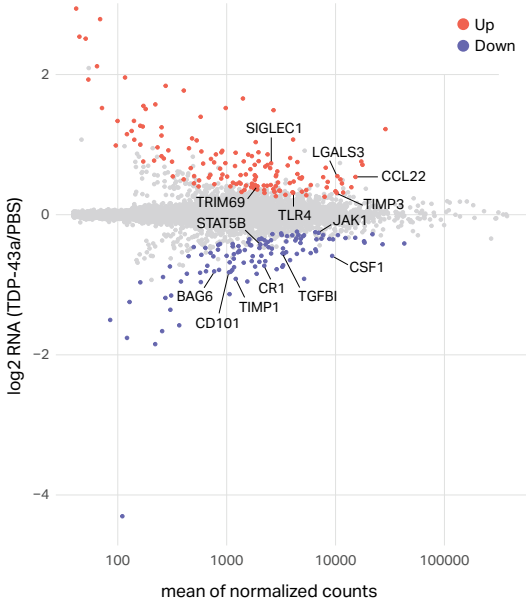

B.

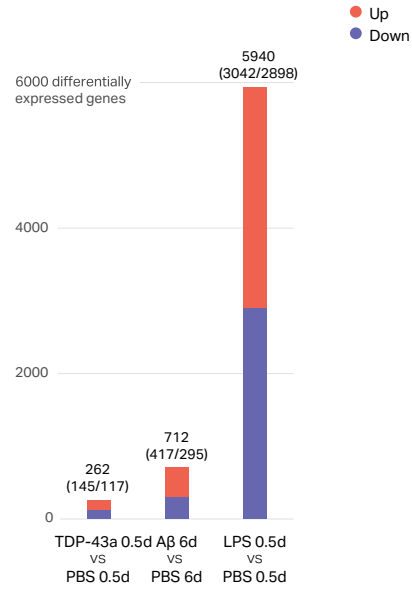

C.

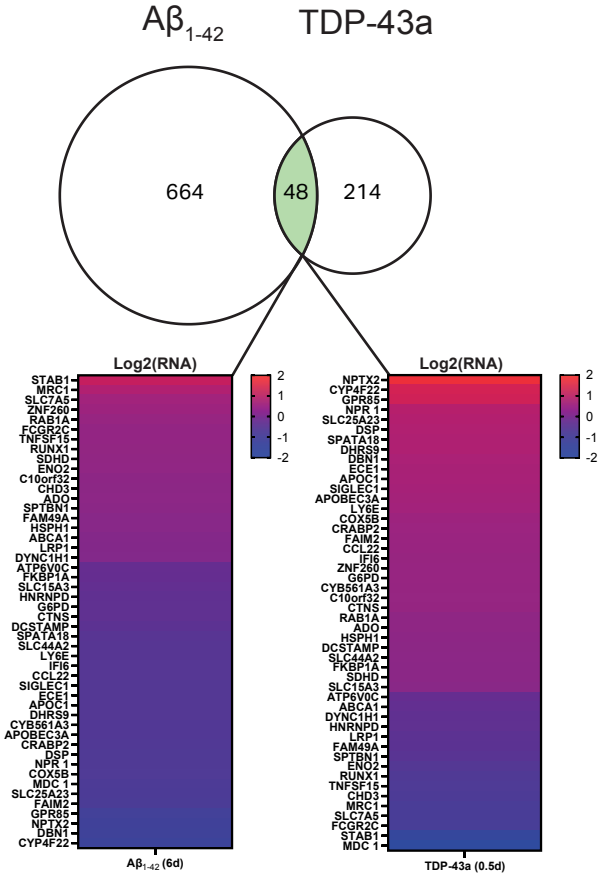

D.

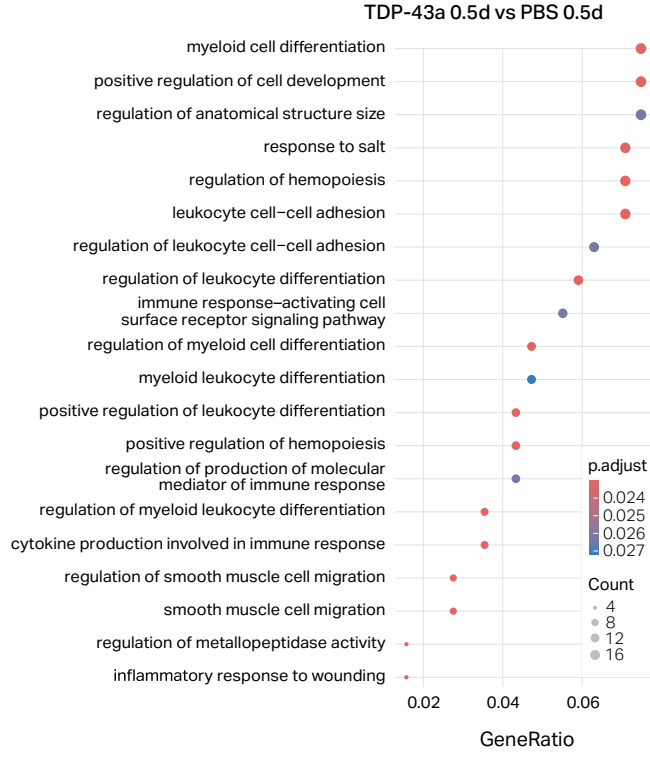

Figure 4

Evangelista et al., 2024

A.

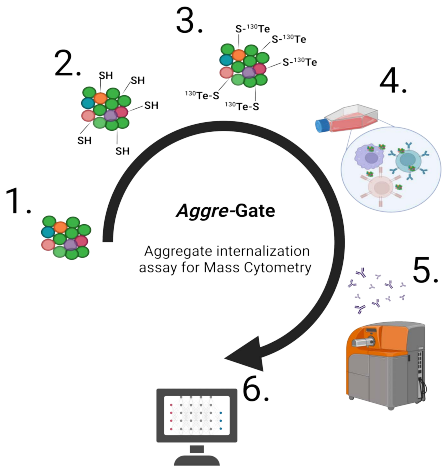

B.

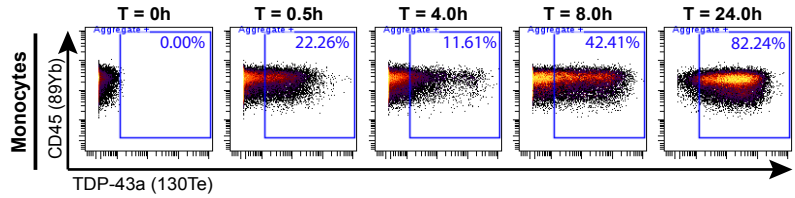

C.

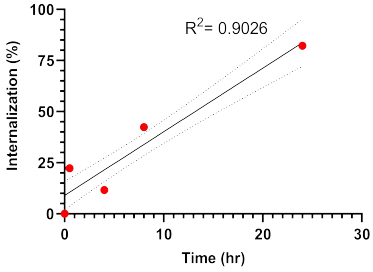

D.

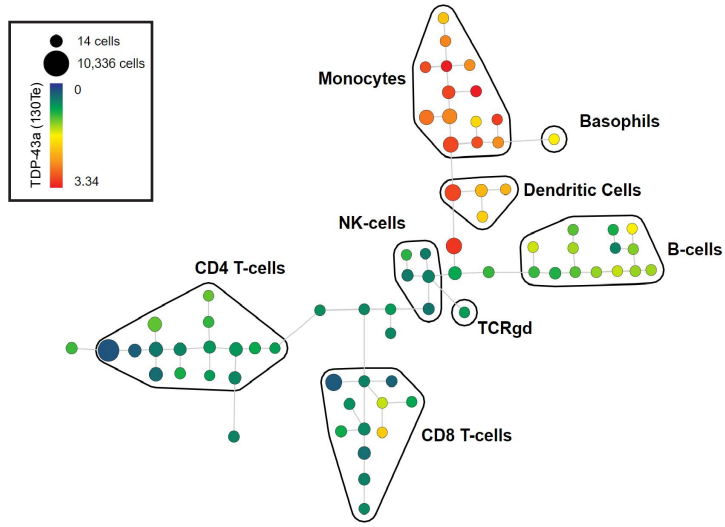

E.

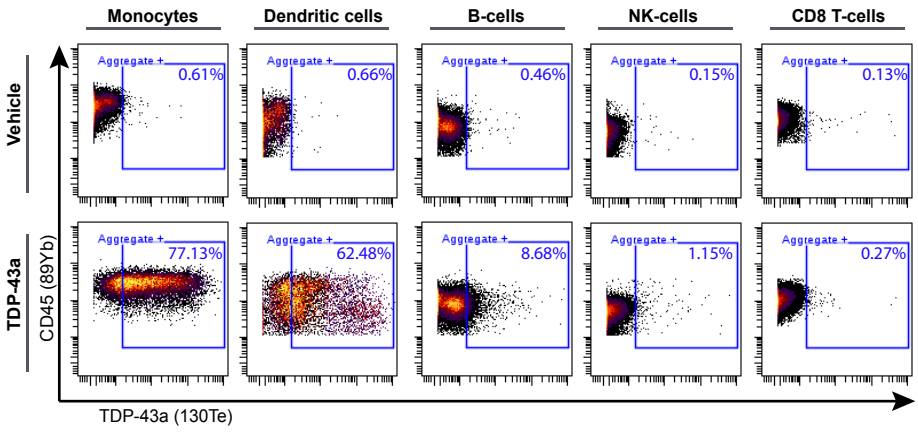

F.

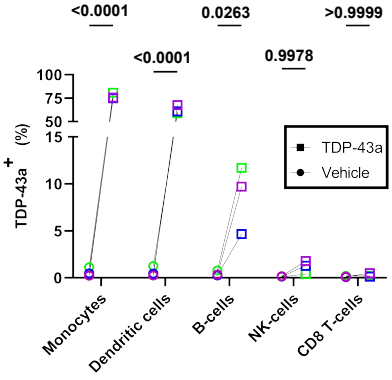

G.

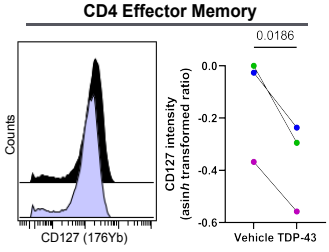

H.

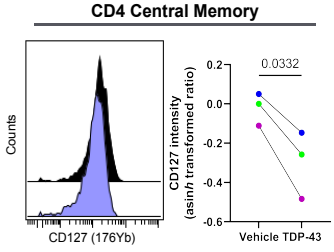

I.

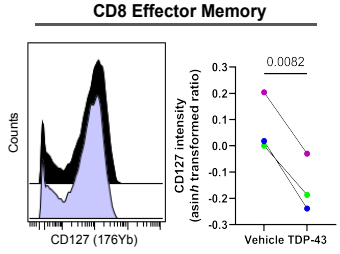

J.

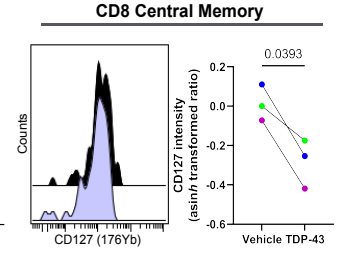

Figure 5

Evangelista et al., 2024

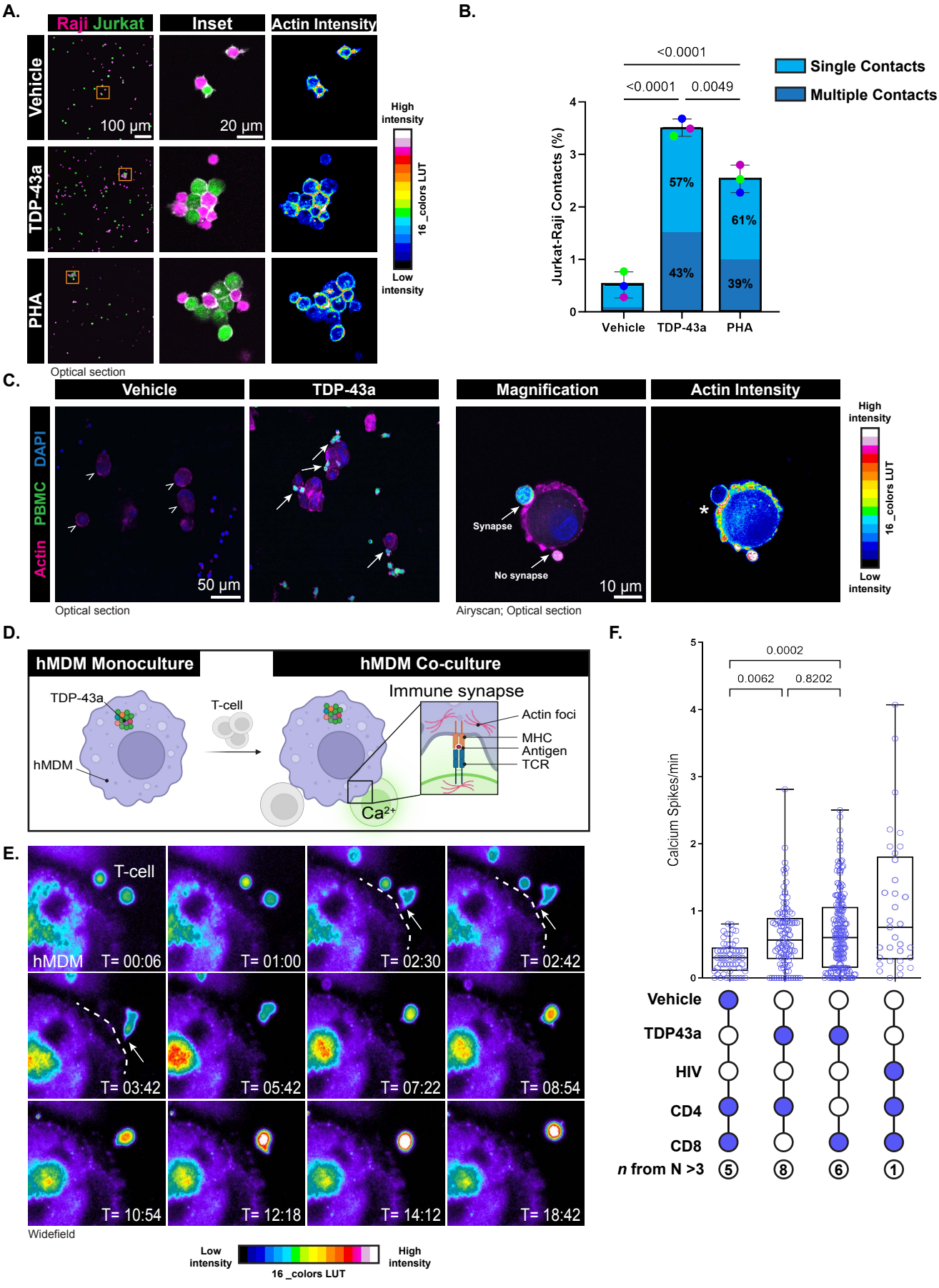

Figure 6

Evangelista et al., 2024

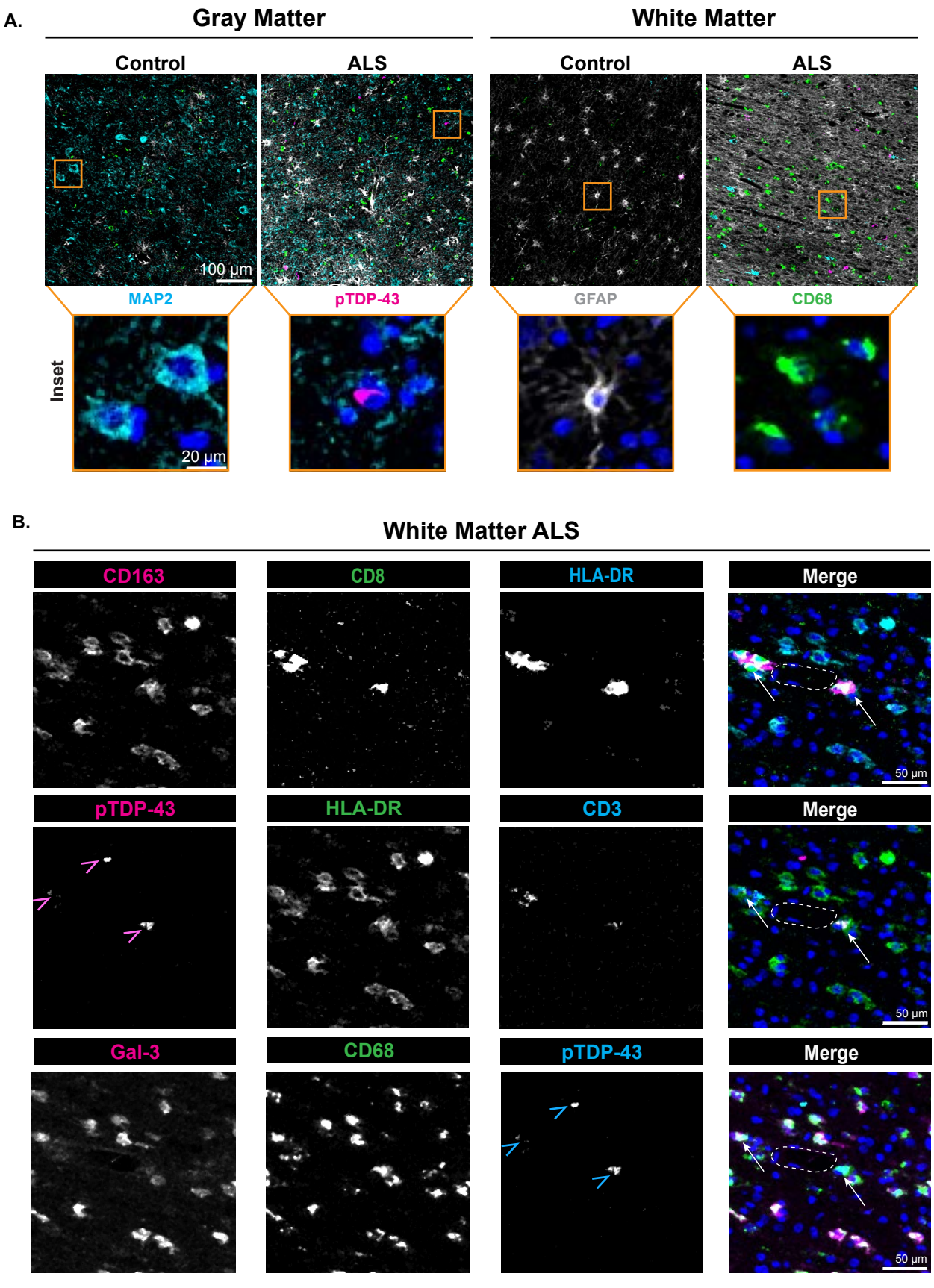

Figure 7

Evangelista et al., 2024

A.

ALS Whole-blood Immune Profiling

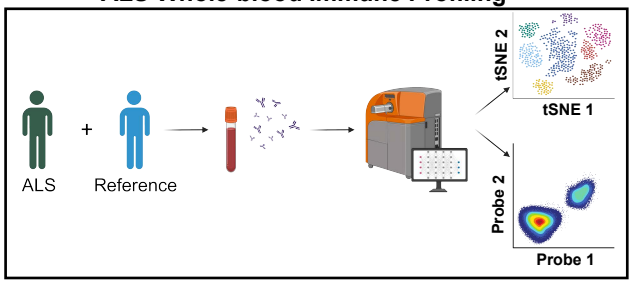

Classifier	Slow	Standard	Fast
$\frac{\Delta ALSFRS\text{-}R}{t}$	$0 < x \leq 0.5$	$0.5 < x \leq 1.0$	$1.0 < x$
N	9	7	6

B.

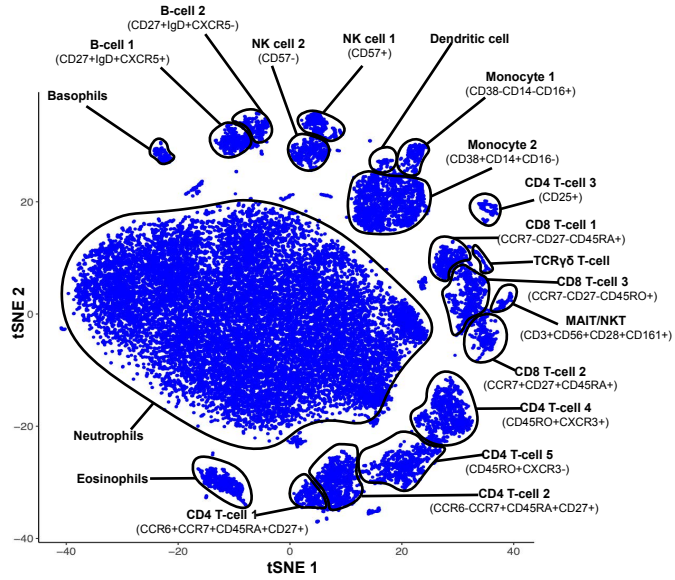

C.

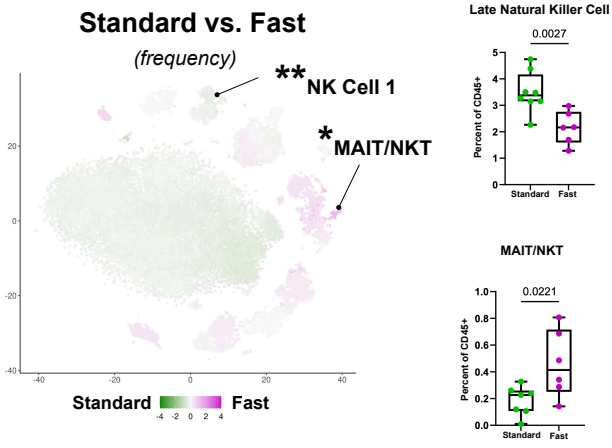

D.

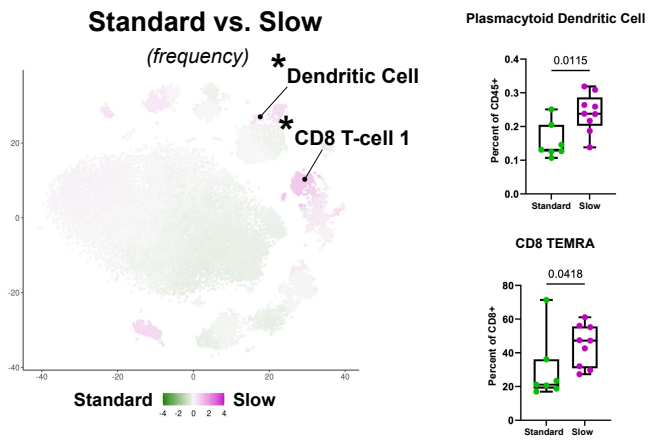

E.

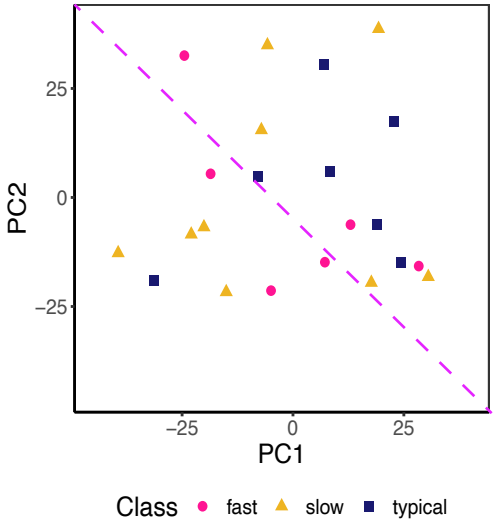

F.

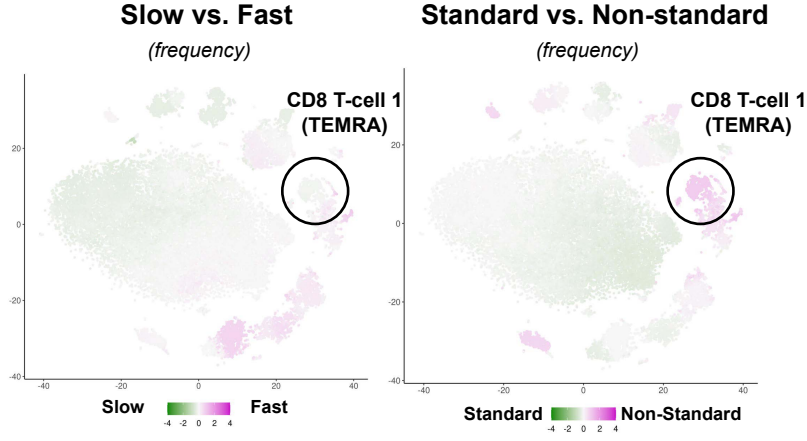

Figure 8

Evangelista et al., 2024

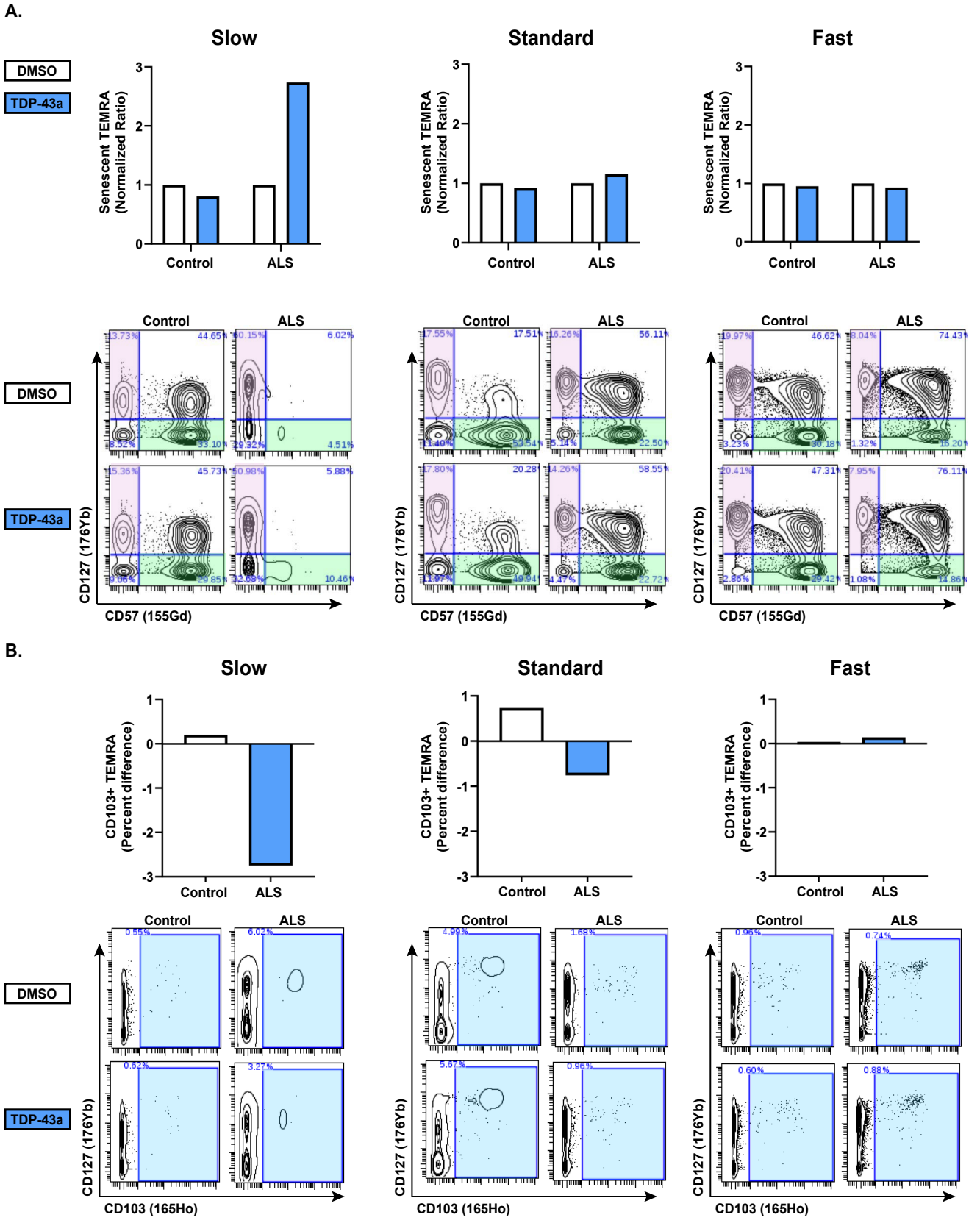

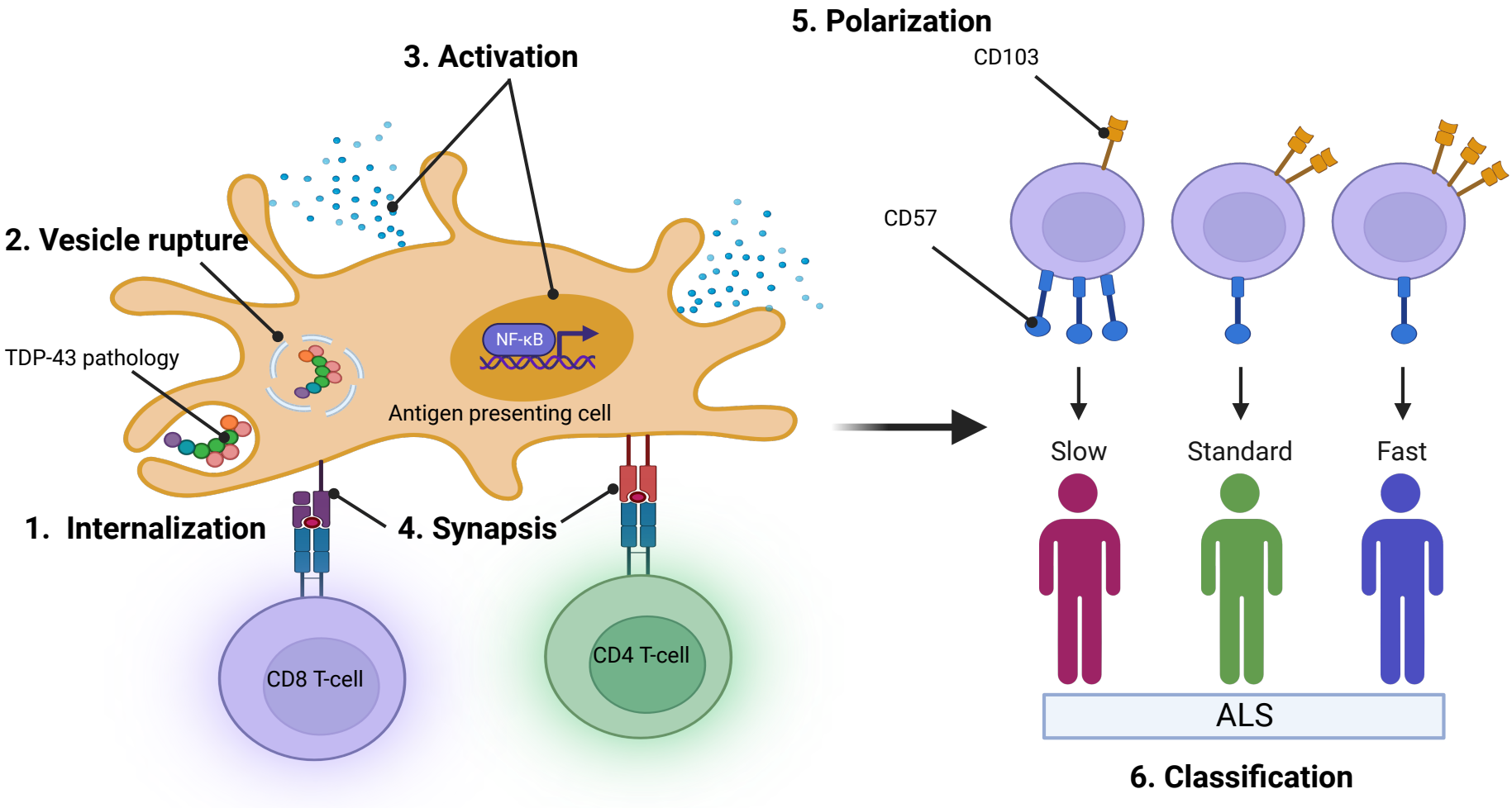
5. Polarization
3. Activation
CD103
2. Vesicle rupture
CD57
TDP-43 pathology
NF-κB
Antigen presenting cell
Slow
Standard
Fast
1. Internalization
4. Synapsis
CD8 T-cell
CD4 T-cell
ALS
6. Classification